Available online at www.sciencedirect.com

SCIENCE @ DIRECT®

International Journal of Solids and Structures 42 (2005) 1849–1881

INTERNATIONAL JOURNAL OF SOLIDS and STRUCTURES

www.elsevier.com/locate/ijsolstr

Numerical modelling of nonlinear response of soil. Part 1: Constitutive model

X. Liu [*], X.H. Cheng, A. Scarpas, J. Blaauwendraad

Faculty of Civil Engineering and Geosciences, Section of Structural Mechanics, Delft University of Technology, Stevinweg 1, 2628 CN Delft, The Netherlands

Received 14 September 2004
Available online 27 October 2004

Abstract

In this contribution, on the basis of the hierarchical approach [Desai, C.S., 1980. A general basis for yield, failure and potential functions in plasticity. International Journal for Numerical and Analytical Methods in Geomechanics 4 (1980) 361–375], a constitutive model for the soil response in the elastoplastic range has been developed. The emphasis has been placed on presenting the particular model characteristics, simulation of soil hardening and softening response and the establishment of model nonassociativity. Based on standard available laboratory triaxial tests, a general procedure has been developed for determination of the material parameters of the constitutive model. All model parameters have been associated with quantities that can be determined from the experimental process ensuring thus the physical meaning of the parameters. A companion paper focuses on the applications of this constitutive model to investigate strain localization phenomena in sand, and the role of the fluid components on strain localization in 3D saturated sand specimen is addressed.

Keywords: Constitutive model; Soil hardening and softening; Flow surface; Parameters; Model verification; Triaxial test; Stress path

---

1. Introduction

In the finite element analysis of geotechnical problems, the choice of an appropriate constitutive model may have a significant influence on the numerical results. The constitutive model should be able to capture the main features of the mechanical behaviour of geomaterials under complex states of stress.

---

[*] Corresponding author. Tel.: +31 15 2787918; fax: +31 15 2785767.
E-mail address: x.liu@ct.tudelft.nl (X. Liu).

0020-7683/$ - see front matter © 2004 Elsevier Ltd. All rights reserved.
doi:10.1016/j.ijsolstr.2004.09.009

In recent years, various types of constitutive models have been developed. Some of them appear to be rather complex however, difficult to relate to material physical behaviour, while other models use parameters that cannot be obtained from common laboratory tests.

Based on the concept of state boundary surface, modified and refined forms of cap models for geological materials were proposed by DiMaggio and Sandler (1971) and later by Baladi and Rohani (1979). Initially the cap model was developed for sands and now has been successfully extended to other materials, such as clays and rocks. Since the cap intersects the hydrostatic axis perpendicularly, this ensures that a state of hydrostatic stress will cause only volumetric plastic deformation when associated plasticity theory is applied.

Lade and Duncan (1975) have developed the isotropic elastic–plastic work hardening model for a cohesionless soil. The model contains subsequent flow surface and a failure surface. The flow surface enclosed by the failure surface has the same general surface as the failure surface, except for the differences in its hardening parameters and its isotropic expansion around the hydrostatic axis. Instead of flow surface with straight meridian line, Lade (1977) modified this model with the cap type of flow surface. The size of the cap type of the flow surface is controlled by the plastic strains occurring during isotropic compression. It is assumed that during material hardening, both the failure surface and the yield cap expand. This model has been examined to some extent for the prediction of soil and pore pressures in undrained triaxial compression tests on saturated sand by Lade (1978). A double hardening model consisting of shear and volumetric loading surfaces was established by Vermeer (1978) for the modelling of initial loading, unloading and reloading of sand.

One of the main stumbling blocks of the classical plasticity theory based on associative flow rules and commonly utilized flow surfaces like Druker–Prager or Coulomb is the overprediction of dilation. It became therefore necessary, therefore to extend classical plasticity ideas to a non-associated form in which the plastic potential functions and flow surface are defined separately (Davis, 1968).

Iwan (1967) extended the formulation of the classical incremental theory of plasticity and assumed work-hardening behaviour and a non-associated flow rule. Instead of using a single flow surface, he postulated a series of nested flow surfaces with each surface translating independently in a purely kinematic manner. The same concept of using a series of nested flow surfaces was also proposed independently by Mróz (1967).

Every constitutive model discussed here has its advantages and its limitations. One model on its own cannot adequately reproduce the behaviour of all soil materials under all conditions. A particular constitutive model for engineering analyses should be chosen, based on the criterion that all the important mechanical characteristics of the material under engineering conditions can be captured. An appropriate constitutive model should be able to reflect the key characteristics of material experimental results. The mathematical relationship of the model should be defined by parameters that can be determined from standard test data. The constitutive formulation should result in a unique and stable stress–strain relationship.

In this contribution, on the basis of the hierarchical approach proposed by Desai (1980), constitutive models are developed to simulate the elastoplastic characterization of geomaterials (i.e. sand). The hierarchical approach permits evolution of models of progressively higher order from the basic constitutive equation representing associative behaviour. Higher order models are obtained by applying a perturbation or correction to the basic constitutive equation (Desai et al., 1986). Hence, many of the most important mechanical characteristics of geotechnical materials such as isotropic and anisotropic hardening, softening, pressure sensitivity, associated and nonassociated plasticity can be captured through this approach. The constitutive models are general and sufficiently simplified in terms of number of material parameters and every parameter has a clear physical meaning.

In general, the proposed constitutive model is applicable for any frictional material. However, in this contribution, only geomaterials are considered. The emphasis is placed on the presentation of the model characteristics in both the hardening and the softening ranges of response, and the establishment of model nonassociativity. The general procedure of model parameters determination is presented. The model is calibrated on the basis of triaxial test results (Cheng et al., 2001) on "Eastern Scheldt" sand. Comparisons of model predictions and laboratory measurements for various stress paths are presented.

2. Basic associative model

As indicated earlier, every constitutive model has its advantages and limitations. One of the major limitations of commonly used cap and critical state models, is that the yielding is controlled by two separate yield functions that intersect each other with a slope discontinuity. In associated plasticity theory, the incremental plastic strain is assumed to be normal to the flow surface at the loading point. Thus, in case of two intersecting flow surfaces, the direction of the incremental plastic strain is not defined uniquely at the point of surface intersection. Thus the volumetric and shear response of the material cannot be properly predicted.

The single surface plasticity model proposed by Desai (1980) includes most of the currently common used plasticity models as special cases. The surface is continuous (smooth) and hence avoids the above mentioned discontinuity problems of multi-surface models.

The form of the model yield function is given by

$$F = \frac{J_2}{p_a^2} - \left[-\alpha \cdot \left(\frac{I_1 + R}{p_a}\right)^n + \gamma \cdot \left(\frac{I_1 + R}{p_a}\right)^2\right] \cdot F_s = 0 \tag{1}$$

where I_1 and J_2 are first and second stress invariants respectively, p_a is the atmospheric pressure with units of stress, Parameter R represents the triaxial strength in tension, F_s is the function related to the shape of the flow surface in the octahedral plane,

$$F_s = (1 - \beta \cdot \cos 3\theta)^m \tag{2}$$

where $\cos 3\theta$ is defined as

$$\cos 3\theta = \frac{3\sqrt{3}}{2} \cdot \frac{J_3}{J_2^{3/2}} \tag{3}$$

in which J_3 is the third invariant of the deviatoric stress and θ is equivalent to the Lode angle. The value of m in Eq. (2) is a material constant that is found to be equal to -0.5 for many geologic materials.

In standard soil triaxial tests, $I_1 + R = (\sigma_1 + 2\sigma_3) = 3 \cdot p'$ and $\sqrt{J_2} = (\sigma_1 - \sigma_3)/\sqrt{3} = q/\sqrt{3}$. Therefore, the yield function in Eq. (1) can be written also in terms of effective mean normal stress p' and deviator stress q as

$$F = \frac{q^2}{3p_a^2} - \left[-\alpha \cdot \left(\frac{3p'}{p_a}\right)^n + \gamma \cdot \left(\frac{3p'}{p_a}\right)^2\right] \cdot F_s = 0 \tag{4}$$

where α, β, γ and n in Eqs. (1) and (2) are material parameters.

Isotropic hardening/softening is described by means of parameter α. The values of α control the size of the flow surface. It is typically defined as a function of deformation history. As α decreases, the size of the flow surface increases, Fig. 1. When $\alpha = 0$, the ultimate stress response surface of the material is attained.

The value of n determines the apex of the flow surface on the $I_1 - \sqrt{J_2}$ or $p' - q$ space. Parameter n is related to the state of stress at which the material response changes from compaction to dilation. Its influence on the geometric characteristics of the surface is portrayed in Fig. 2. It is worth noticing that not only the shape but also the size of the surface is influenced as well.

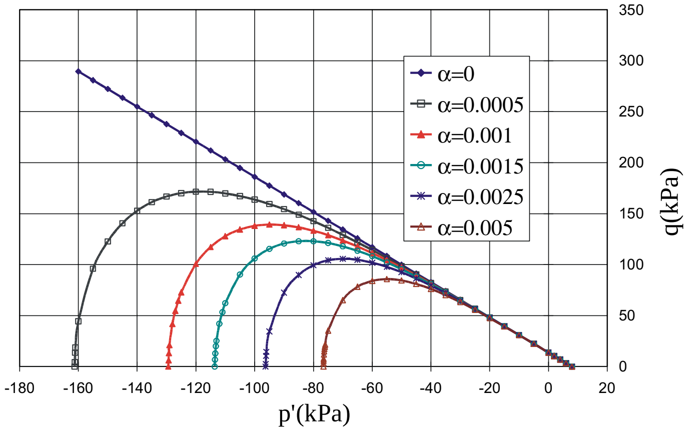

Fig. 1. α influences on F in $p' - q$ space.

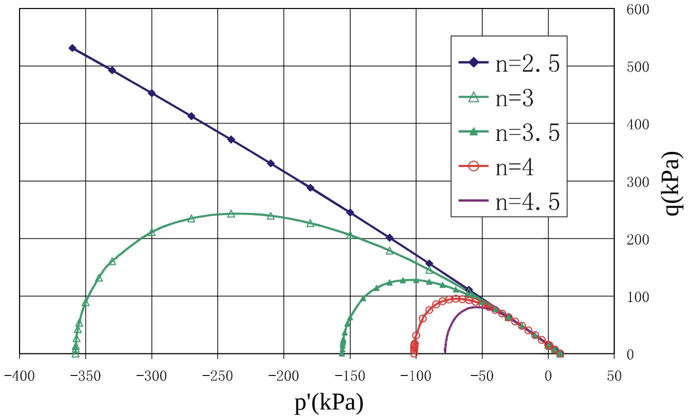

Fig. 2. n influences on F in $p' - q$ space.

Parameter γ is related to the ultimate strength of the material. It denotes the slope of the ultimate stress response surface. Parameter β is related to the trace of the flow surface on the octahedral plane. For $\beta = 0$ the trace is circular, Fig. 3(a). As β increases, the trace progressively becomes triangular, Fig. 3(b). The value of β should be less than or equal to 0.76 for the required convex surface. It is possible that some materials may exhibit concave yield surfaces, i.e. $\beta > 0.76$, however, such materials are not considered herein.

By defining β as a function of I_1, it is possible to change the trace of the surface with confinement. For some cementitious materials this is advantageous since experimental evidence indicates that for low confinement levels the shape of the surface on the octahedral plane is triangular while for higher levels of confinement it tends to circular.

According to experimental observations, for a stress path sensitive material, the ultimate stress response surface of some geomaterials is not always a straight line on the $I_1 - \sqrt{J_2}$ or $p' - q$ space, but a curved one. γ can vary under different stress path. These will lead the numerical model can not capture mechanical characteristics of the material under complicated engineering conditions. In order to enhance the applicability of the classical yield function in Eq. (1), a modified form of the yield function is proposed and expressed in Eq. (5). The benefit of choosing modified form of the yield function can be observed in the model verifica-

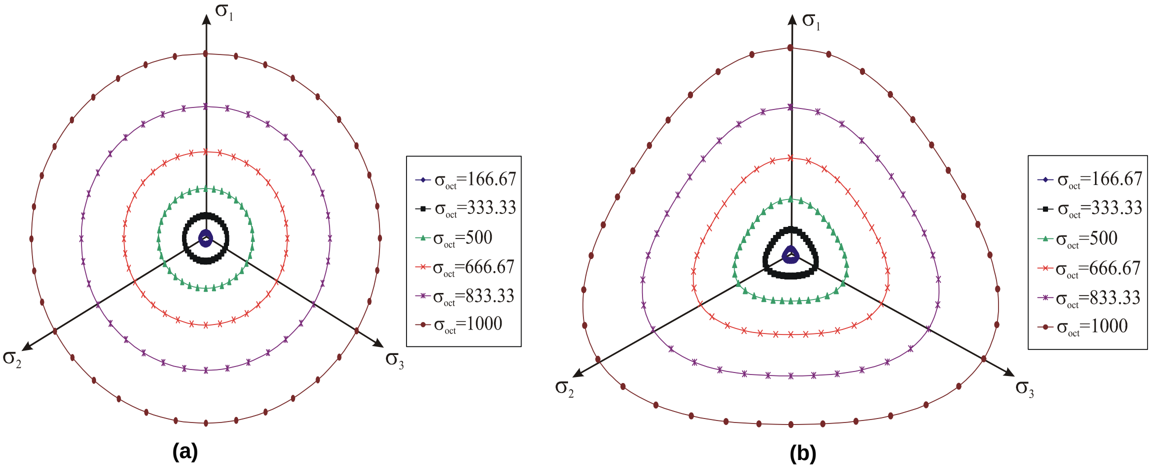

(a) **(b)**

Fig. 3. Plot of the F on the octahedral plane with different β values.

tion part. The modification of the classical yield function is done by replacing the power 2 in Eq. (1) with the parameter g:

$$F = \frac{J_2}{p_a^2} - \left[-\alpha \cdot \left(\frac{I_1 + R}{p_a} \right)^n + \gamma \cdot \left(\frac{I_1 + R}{p_a} \right)^g \right] \cdot F_s = 0 \tag{5}$$

Similar as Eq. (4), the modified yield function in Eq. (5) can be written also in terms of effective mean normal stress p' and deviator stress q as

$$F = \frac{q^2}{3p_a^2} - \left[-\alpha \cdot \left(\frac{3p'}{p_a} \right)^n + \gamma \cdot \left(\frac{3p'}{p_a} \right)^g \right] \cdot F_s = 0 \tag{6}$$

In Eq. (5) or (6), the parameter g controls the shape of the stress response surface of the material. The influence of g on the ultimate stress response surface in $p' - q$ space is presented in Fig. 4(a) and (b). It can be observed that, when $g < 2$, the ultimate stress response surface becomes a bullet shape surface, see Fig. 4(a), and when $g > 2$, it becomes a trump shape surface, Fig. 4(b). If $g = 2$ the classical ultimate stress

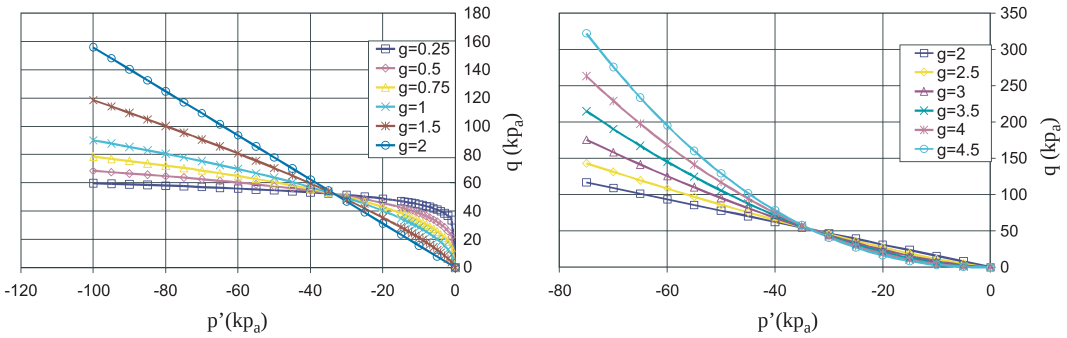

(a) $g \leq 2$ **(b)** $g \geq 2$

Fig. 4. g influences on F in $p' - q$ space.

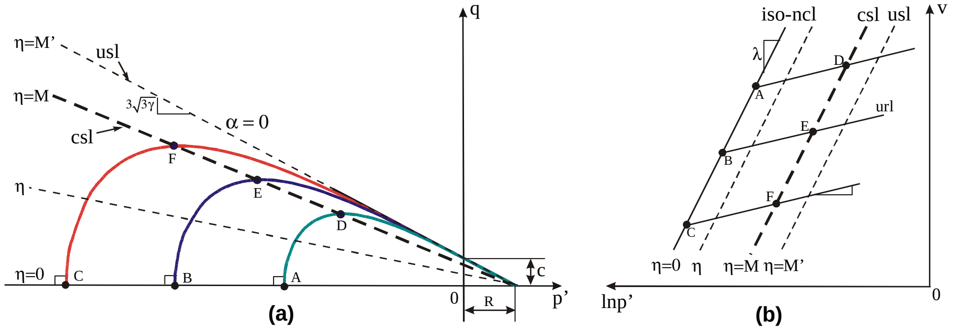

Fig. 5. Schematic of the flow surface, the usl and the csl in (a) $p' - q$ space and (b) compression plane.

response surface is attained. At the material ultimate stress state, by employing a least square procedure on Eq. (5) or Eq. (6), parameter g can be determined. In this study, all the model parameters will be derived on the basis of the modified form of the yield function.

2.1. Flow surface characteristics

Fig. 5(a) shows a schematic of the classical flow surface in the $p' - q$ space. It is observed that the flow surface is continuous and convex in the stress space. The convex shape of the surface means that positive incremental plastic work is produced by an increment of stress resulting thus to a material with stable plasticity response (Drucker, 1951). For triaxial compression states, the tip of the flow surface intersects the p' axis perpendicularly. This is necessary for ensuring that a state of pure hydrostatic stress will cause only volumetric plastic deformation.

When $\alpha = 0$, the intersection of the flow surface with the negative hydrostatic axis p' is at infinity. This is named the material ultimate stress state. The locus of the ultimate stress state in the $p' - q$ space is defined by a line with peak stress ratio $\eta = q/p' = M'$ in which q and p' are the deviatoric stress and effective mean normal stress at material ultimate stress state, respectively. This line is called the ultimate state line (usl) and it represents the maximum response in the stress–strain curves obtained from various stress paths.

Another important feature of the model is that for $\alpha \neq 0$ the locus of the apexes of the flow surface represents states of zero volume change after which the material starts to dilate. These states have been named characteristic states. [1] The line (with stress ratio $\eta = M$ in Fig. 5(a)) that connects these states is called the critical state line (csl) in the critical state model and it separates the stress space into compression and dilation regions. In the critical state model, once the state of stress has reached the critical state line, any subsequent deformation of the material can occur without changes in volume.

Fig. 5(b) presents some characteristics of the model in the v–lnp' plane with v being the specific volume. In this plane, which is also known as the "compression plane", for a given value of the stress ratio $\eta = q/p'$, the interrelation between the experimentally measured specific volume v and the logarithm of pressure is plotted. For example, for a fully isotropic compression test, points A, B and C of Fig. 5(a) are plotted along the line indicated as iso-ncl (i.e. isotropic normal compression line) in Fig. 5(b). Points D, E and F corresponding to the csl of Fig. 5(a) are also shown in Fig. 5(b).

---

[1] Even though this state is physically identical to the critical state of the model proposed by Roscoe et al. (1963), Luong (1982) and Ibsen and Lade (1998), have named it "characteristic state".

In the case of isotropic compression, upon unloading, the relation between p' and v is indicated by the unloading reloading line (url), Fig. 5(b). The point of intersection of this line with the v axis indicates the magnitude of the permanent volumetric deformation corresponding to the magnitude of the imposed isotropic compression, i.e. A, B or C in Fig. 5.

According to Ibsen and Lade (1998), different deformation mechanisms are active in the two subspaces in which the csl divides the stress space. Below the csl, the resistance to deformation is governed by sliding friction due to the surface roughness of the particles or by the interlocking friction between particles. In the subspace situated between the usl and the csl, the resistance to deformation is governed by disrupture of interlocking and volumetric dilation.

When loose sand is tested under drained conditions, the volume continuously decreases until zero volume change when the critical state (denoted by *c*) is attained. On the other hand, for dense sand, the material may first decrease in volume until a transient state of zero volume change (denoted also by *c*) is reached at small strain magnitudes and, after that, the material dilates. Finally, beyond the ultimate stress state denoted by *d*, a state of zero volumetric change may again be attained indicated also by *c* in Fig. 6. It can thus be concluded that during triaxial testing of some soil materials, a state of zero volumetric change can be attained more than once.

In regards to material constitutive model, in contrast to the classical critical state model, the constitutive model presented in the following sections is capable of simulating the response of frictional materials exhibiting either type of dilatant behaviour as shown in Fig. 6.

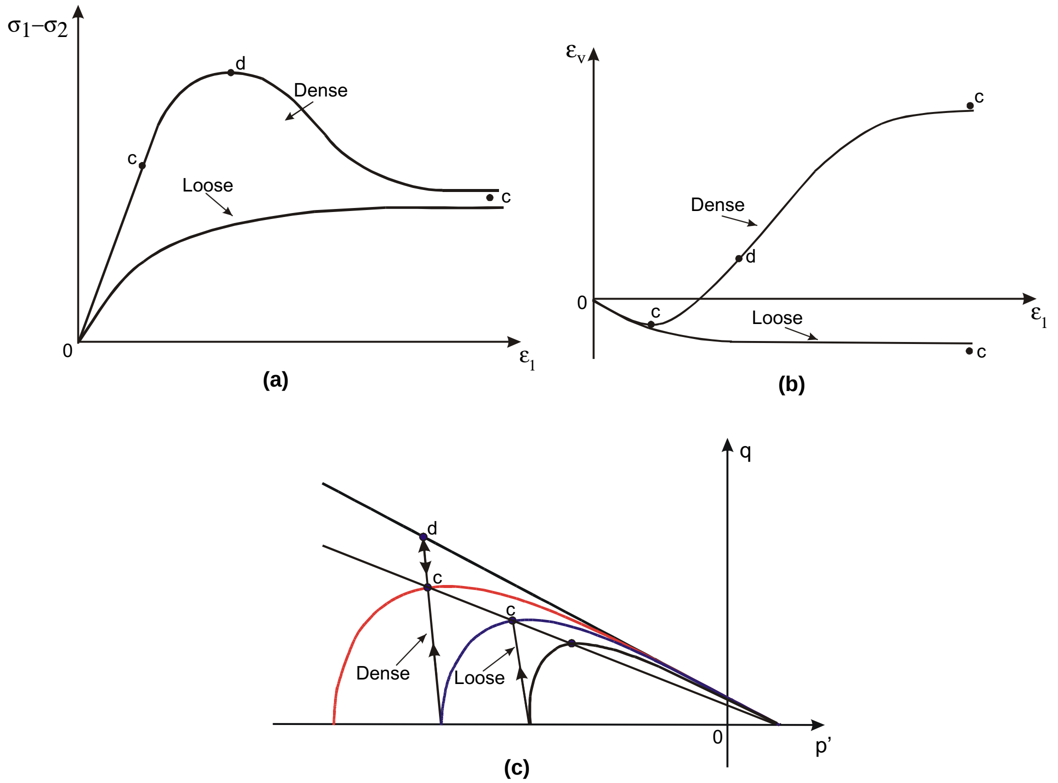

Fig. 6. Schematic stress and deformation in drained triaxial test on loose and dense granular materials.

2.2. Simulation of material hardening and softening behaviour

Most materials can exhibit increase of response beyond the elastic limit. This phenomenon is called hardening, whereas behaviour is called softening when materials show a decrease in strength during progressive straining after the peak strength is reached.

2.2.1. Material hardening

According to experimental evidence, it is generally known that during the process of incremental plastic deformation, the yield surface changes size, shape and location. A law governing this aspect of response is called the hardening rule. The manner in which hardening occurs for geotechnical materials can be quite complicated. For this reason, some simplified assumptions must be made in the view of the numerical implementation.

Mathematically, hardening is characterized by parameters that vary with the plastic loading history. The hardening parameter is often a function of the effective plastic strain or plastic work. There are several hardening rules that have been proposed to describe the growth of subsequent yield surfaces for material hardening. These are: isotropic hardening, kinematic hardening and mixed hardening.

For quasi-static monotonic loading, the isotropic hardening model is appropriate for the representation of material behaviour. In the case of reversals of loading, kinematic or mixed hardening may be more appropriate. In this study only isotropic hardening is considered.

As discussed earlier, parameter α in the model controls the size of the flow surface, Fig. 1. When α decreases, the size of the surface increases and vice versa. According to the theory of plasticity, for an isotropically hardening material, the plastic deformations are associated with expansion of the flow surface. Therefore, parameter α employed here for the constitutive model can be defined as a function of the plastic deformation history. The actual functional form of α should be determined on the basis of laboratory tests.

The parameter α can be typically expressed in terms of internal variables such as the effective plastic strain, the plastic work, the dissipated energy etc. It was found that use of the effective plastic strain provides a more consistent formulation than that of plastic work (Desai, 2001). Also it is relatively easier to compute the effective plastic strain from available test data. Hence α is expressed as

$$\alpha = \alpha(\xi,\ \xi_{\mathrm{v}},\ \xi_{\mathrm{d}}) \tag{7}$$

in which the effective plastic strain ξ is defined on the basis of plastic strain increments $\mathrm{d}\varepsilon_{ij}^{\mathrm{p}}$ as

$$\xi = \int (\mathrm{d}\varepsilon_{ij}^{\mathrm{p}}\mathrm{d}\varepsilon_{ij}^{\mathrm{p}})^{\frac{1}{2}} \tag{8}$$

Obviously, the magnitude of the effective plastic strain ξ never decreases. ξ_{v} and ξ_{d} are the volumetric and deviatoric components of ξ respectively. They can be expressed as

$$\xi_d = \int (\mathrm{d}e_{ij}^{\mathrm{p}} \cdot \mathrm{d}e_{ij}^{\mathrm{p}})^{1/2} \tag{9}$$

$$\xi_{\mathrm{v}} = \int \frac{1}{\sqrt{3}} \cdot (\mathrm{d}\varepsilon_{kk}^{\mathrm{p}} \cdot \mathrm{d}\varepsilon_{kk}^{\mathrm{p}})^{1/2} \tag{10}$$

where $\mathrm{d}e_{ij}$ is incremental deviatoric plastic strain tensor defined as

$$\mathrm{d}e_{ij}^{\mathrm{p}} = \mathrm{d}\varepsilon_{ij}^{\mathrm{p}} - \frac{1}{3}\mathrm{d}\varepsilon_{kk}^{\mathrm{p}} \cdot \delta_{ij} \tag{11}$$

and $\mathrm{d}\varepsilon_{kk}^{\mathrm{p}}$ is the incremental volumetric plastic strain. δ_{ij} is the Kronecker δ.

The relationship between the effective plastic strain ξ and its deviatoric and volumetric components ξ_d and ξ_v can be expressed as

$$\xi = \sqrt{\xi_v^2 + \xi_d^2} \tag{12}$$

In a triaxial test, the corresponding deviatoric and volumetric components ξ_d and ξ_v in Eqs. (9) and (10) can be expressed as

$$\xi_d = \sqrt{\frac{2}{3}} \cdot (\varepsilon_1^p - \varepsilon_2^p) \tag{13}$$

$$\xi_v = \frac{1}{\sqrt{3}}(\varepsilon_1^p + 2\varepsilon_2^p) \tag{14}$$

in which ε_1^p and ε_2^p are the incremental plastic strain in vertical and horizontal directions respectively.

By rearrangement of Eq. (12), the effective plastic strain ξ can be also expressed by

$$\xi = \xi_d\sqrt{1 + \left(\frac{\xi_v}{\xi_d}\right)^2} = \sqrt{\frac{2}{3}} \cdot (\varepsilon_1^p - \varepsilon_2^p) \cdot \sqrt{1 + \frac{1}{2} \cdot \left(\frac{\varepsilon_1^p + 2\varepsilon_2^p}{\varepsilon_1^p - \varepsilon_2^p}\right)^2} = \sqrt{\frac{2}{3}} \cdot (\varepsilon_1^p - \varepsilon_2^p) \cdot \sqrt{1 + \frac{1}{2} \cdot (\sin\psi)^2} \tag{15}$$

where ψ is the dilatancy angle which can be measured from the material volumetric response. Obviously, the effective plastic strain ξ represents physically the accumulation of plastic strain associated with material deviatoric and volumetric plastic deformations.

Several forms of α have been developed for description of the hardening response of various engineering materials (Desai and Faruque, 1984; Desai et al., 1986). Based on laboratory observations for various stress paths, material hardening response is influenced both by the coupled and uncoupled actions from volumetric and deviatoric plastic deformations. For example, in a hydrostatic compression test, since the stress path corresponding to this test remains along the hydrostatic axis, only volumetric plastic deformations are created. On the other hand, for purely shear loading, there will be no volume change and the material will experience only large shear deformations.

In order to take these observations into account, in the framework of this study, parameter α of the modified yield function in Eq. (5) is expressed as a function of both volumetric and deviatoric hardening components, α_v and α_d:

$$\alpha = \eta_h \cdot \alpha_v + (1 - \eta_h) \cdot \alpha_d \tag{16}$$

where

$$\alpha_v = a_1 \cdot e^{b_1 \cdot \xi_v} \tag{17}$$

$$\alpha_d = c_1 \cdot \left[1 - \frac{(M')^2}{27\gamma} \cdot \left(\frac{\xi_d}{d_1 + \xi_d}\right)^2 \cdot \left(\frac{3p_c}{p_a}\right)^{(2-g)}\right] \tag{18}$$

$$\eta_h = \frac{\xi_v}{\xi_v + \xi_d} \tag{19}$$

α_v and α_d are the volumetric and deviatoric hardening components respectively. a_1, b_1, c_1, and d_1 are hardening parameters. The ratio η_h in Eq. (19) denotes the contribution of volumetric hardening to the overall material hardening response.

Details of the derivation of the mathematical expressions for α_v and α_d including the determination of the corresponding hardening parameters will be presented in Section 4. Since the derivation of both expressions

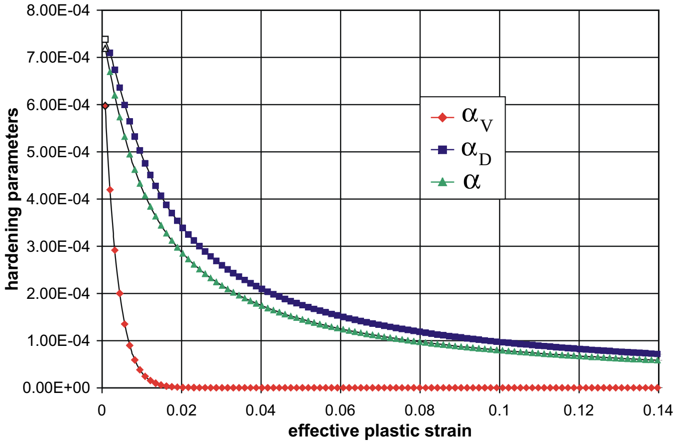

Fig. 7. Variation of α, α_v and α_d with respects to ξ in a CTC test.

is based on laboratory observations, the physical basis of each parameter in the expressions is quite clear and each parameter links directly to the basic soil mechanical characteristics.

It can be observed, when volumetric and deviatoric behaviour are coupled, α can be determined directly by using Eq. (16). For example, in a conventional triaxial compression (CTC) test simulation, Fig. 7 shows the variations of α and its volumetric and deviatoric components α_d and α_d with respect to ξ. Since loading along a CTC test stress path produces relatively more shear deformation than volumetric one, the volumetric hardening function α_v decreases quicker than the deviatoric hardening function α_d.

2.2.2. Material softening

Typical stress–strain behaviour for a soil under compressive loading is shown in Fig. 8(a). This figure indicates that, for deformations beyond those corresponding to the ultimate strength (denoted by *d*), the material undergoes softening (degradation) in its strength and stiffness. Nevertheless, it continues to carry load until it approaches its residual strength at the critical state (denoted by *c*).

Theories of plasticity utilized to deal with the material softening behaviour belong to the continuum mechanics approach. In this contribution, an isotropic measure of response flow surface degradation has been introduced into the model to simulate the softening process. This adaptation of the model is achieved

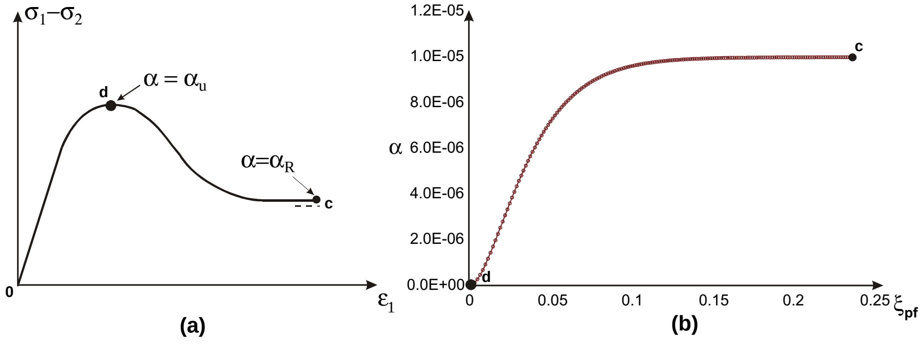

Fig. 8. Stress–strain behaviour and α variation with respect to ξ_{pf}.

by means of specifying the variation of parameter α, after response degradation initiation, as an increasing function of the monotonically varying equivalent post fracture plastic strain ξ_{pf}:

$$\alpha = \alpha_{\mathrm{R}} + \eta_{\mathrm{s}} \cdot (\alpha_{\mathrm{u}} - \alpha_{\mathrm{R}}) \tag{20}$$

in which

$$\eta_{\mathrm{s}} = \mathrm{e}^{-\kappa_1 \cdot \xi_{\mathrm{pf}}} \tag{21}$$

and α_{u} and α_{R} are the values of α corresponding to material ultimate stress response and residual stress state respectively, see Fig. 8(a). The parameter κ_1 is a material parameter that determines the material degradation rate. The definition of ξ_{pf} is similar to the effective plastic strain ξ defined in Eq. (8). The difference is that only incremental plastic strains after response degradation initiation are now taken into account.

The variation of α as a function of ξ_{pf} is shown in Fig. 8(b). At material degradation initiation, due to rapid material softening, α increases quickly. As the state of residual response is approached, the variation of α becomes insignificant and softening gradually ceases.

By relating α to a physically measurable quantity like the plastic strains, its functional form can be determined on the basis of laboratory tests. Also, with this simplified approach, only one parameter κ_1 needs to be determined to characterize the material softening response.

3. Nonassociative model

The physical soil characteristics such as density, void ratio, water content and mineralogy can greatly influence soil behaviour. Successful prediction of soil response depends on whether the material model used can capture the significant characteristics of response under engineering conditions. The most significant characteristics of soil response are the ultimate strength, the dilation or contraction, the hardening or softening response and the stress path dependence.

In the theory of plasticity, the direction of the incremental plastic strain is defined by the plastic potential function Q. If the potential and flow functions coincide with each other, the incremental plastic strain is then proportional to the gradient of the yield function F and the flow rule is called ‘‘associated’’. Otherwise, if the plastic potential function Q and the yield function F are defined separately, the flow rule is called ‘‘nonassociated’’. In this case, the yield function F controls whether plastic deformations occur, while the direction of the incremental plastic strain is evaluated on the basis of the plastic potential Q.

Both associated and nonassociated flow rules are commonly used with plasticity models for geotechnical materials. For some materials such as metals and undrained cohesive soils, the use of the associated flow rule is most common. On the other hand, for some frictional and cohesionless soils, material models incorporating the associated flow rule usually exhibit plastic dilation that is larger than the one that is observed in laboratory testing. In this case, it is necessary to employ a nonassociative flow rule for plasticity modelling.

In literature, several examples can be found of utilization of nonassociative rules to study the nonlinear response of soil. For example, Poorooshasb et al. (1965) indicated that the incremental plastic strains obtained from experimental results are not normal to the yield surface. Lade (1977), Prevost (1985) and Lacy and Prevost (1987) assumed that the deviatoric components of plastic strain are normal to the deviatoric trace of the failure surface. Lade et al. (1987, 1988) have discussed the consequences of using nonassociated flow rules with geological materials.

In the hierarchical approach (Desai, 1980), a nonassociative model is obtained by defining the potential function as a correction/modification to the yield function. This correction approach can be used to develop models of various grades for characteristics such as associative and isotropic hardening, nonassociative, isotropic and anisotropic hardening and strain softening response. In this study, focus is placed on nonassociative isotropic hardening and softening features.

By utilizing the notion of correction of the yield function, the potential function Q is expressed as

$$Q = F + h(I_1, J_i, \xi) \tag{22}$$

in which F is the modified yield function defined in Eq. (5), $h(I_1, J_i, \xi)$ is a correction function of stress invariants I_1, $J_i (i = 2,3)$ and ξ is the effective plastic strain defined in Eq. (8).

In the constitutive model, the size of Q is controlled by a hardening/softening parameter α_Q defined as

$$\alpha_Q = \alpha + \alpha_c \tag{23}$$

in which α_c is a correction function expressed as

$$\alpha_c = \kappa_c(\alpha_0 - \alpha)(1 - \chi_v) \tag{24}$$

determined on the basis of experimental evidence. The parameter α_0 in Eq. (24) is the value of α at the initiation of nonassociativeness.

In a soil triaxial test, the initiation of nonassociativeness may be assumed to occur after the hydrostatic compression. Otherwise, α_0 corresponds to the value of α at initiation of plastic response. The parameter χ_v controls the contribution of volumetric plastic deformation to the expansion of the potential surface and is defined by

$$\chi_v = \frac{\xi_v}{\xi} \tag{25}$$

where ξ_v is the volumetric component of effective plastic strain ξ. The parameter κ_c in Eq. (24) is the only extra material parameter that needs to be determined to capture material nonassociative behaviour.

Thus, the plastic potential Q in Eq. (22) is written in $I_1 - J_2$ space as

$$Q = \frac{J_2}{p_a^2} - \left[-\alpha_Q \cdot \left(\frac{I_1 + R}{p_a} \right)^n + \gamma \cdot \left(\frac{I_1 + R}{p_a} \right)^g \right] \cdot F_s \tag{26}$$

where F_s is defined in Eq. (2). Similarly Eq. (26) can be also expressed in $p' - q$ space as

$$Q = \frac{q^2}{3p_a^2} - \left[-\alpha_Q \cdot \left(\frac{3p'}{p_a} \right)^n + \gamma \cdot \left(\frac{3p'}{p_a} \right)^g \right] \cdot F_s \tag{27}$$

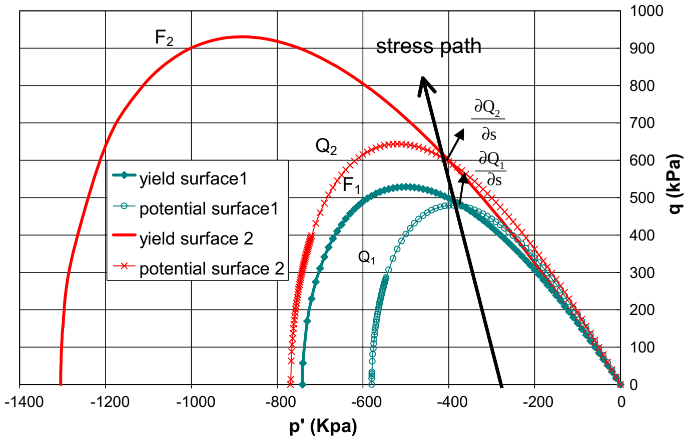

Fig. 9. Schematic of flow and plastic potential surfaces.

It can be observed that for isotropically hardening material subject to hydrostatic compression loads, $\chi_{\mathrm{v}} = 1$ in Eq. (25) and hence $\alpha_Q = \alpha$ in Eq. (23). This means that nonassociativeness does not occur under a hydrostatic compression condition. For the case of $\kappa_{\mathrm{c}} = 0$, the potential function Eq. (26) yields $Q = F$ indicating that the associative model is a special case of the nonassociative one.

Fig. 9 illustrates the basic notion of the proposed model. As shown, to every point along the stress path correspond a yield F_i and a potential surface Q_i. The incremental plastic strain vector along the stress path is shown as normal to the potential surfaces. Depending on the direction of the incremental plastic strain vector, soil plastic dilation or contraction is predicted.

In the model verification, the benefits of using this nonassociative model to simulate the mechanical response of Eastern Scheldt sand are shown.

4. Model parameters determination procedure

The accuracy of any numerical simulation depends on the capabilities of the constitutive model but, also, on the quality of the associated material parameters. In this section emphasis is placed on the general procedure for the determination of the material parameters of the constitutive model presented in the foregoing sections. The model is calibrated on the basis of triaxial test results (Cheng et al., 2001) on "Eastern Scheldt" sand. Comparisons of model predictions and laboratory measurements for various stress paths are presented.

4.1. Parameters β, γ and R

At material ultimate stress state, $\alpha = 0$, the yield function in Eq. (5) can be written as

$$\frac{J_2}{p_{\mathrm{a}}^2} - \gamma \cdot \left(\frac{I_1 + R}{p_{\mathrm{a}}}\right)^{g} \cdot (1 - \beta \cdot \cos 3\theta)^{-1/2} = 0 \tag{28}$$

which can be expressed in terms of deviator stress q and effective stress p' as

$$q = p_{\mathrm{a}} \cdot \sqrt{3\gamma} \cdot \left(\frac{3p'}{p_{\mathrm{a}}}\right)^{g/2} (1 - \beta \cos 3\theta)^{-1/4} \tag{29}$$

Obviously, in Eq. (29) two parameters γ and β are required for defining the material ultimate response.

To obtained the parameters γ and β, two tests are necessary. One is the triaxial compression (TC) test and the other is the triaxial extension (TE) test. During triaxial compression tests, the stress paths are in the radial direction at Lode angle $\theta = 0°$, hence Eq. (29) can be written as

$$q_{\mathrm{TC}} = p_{\mathrm{a}} \cdot \sqrt{3\gamma} \cdot \left(\frac{3p'_{\mathrm{TC}}}{p_{\mathrm{a}}}\right)^{g/2} (1 - \beta)^{-1/4} \tag{30}$$

Similarly, during TE tests, the stress paths are in the radial direction at Lode angle $\theta = 60°$, hence Eq. (29) can be expressed as

$$q_{\mathrm{TE}} = p_{\mathrm{a}} \cdot \sqrt{3\gamma} \cdot \left(\frac{3p'_{\mathrm{TE}}}{p_{\mathrm{a}}}\right)^{g/2} (1 + \beta)^{-1/4} \tag{31}$$

Fig. 10 shows a schematic of the ultimate surface on $p' - q$ space for $g = 2$ in the yield function. The slope of the ultimate surface varies with the stress paths. In the TC stress path, the slope is equal to $3\sqrt{3\gamma} \cdot (1 - \beta)^{-1/4}$ and in the TE test the slope is equal to $3\sqrt{3\gamma} \cdot (1 + \beta)^{-1/4}$.

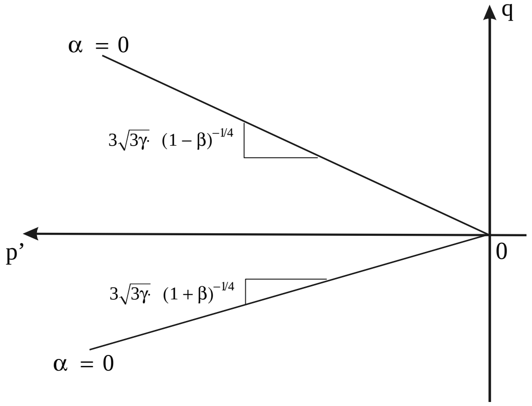

Fig. 10. Schematic of the Failure Surface on $p' - q$ space.

Considering Eqs. (30) and (31), the parameter β can be expressed as

$$\beta = \frac{\left(\frac{q_{\mathrm{TC}}}{q_{\mathrm{TE}}}\right)^4 - \left(\frac{p'_{\mathrm{TC}}}{p'_{\mathrm{TE}}}\right)^{2g}}{\left(\frac{q_{\mathrm{TC}}}{q_{\mathrm{TE}}}\right)^4 + \left(\frac{p'_{\mathrm{TC}}}{p'_{\mathrm{TE}}}\right)^{2g}} \tag{32}$$

Using Eqs. (30) and (31), parameter γ can be computed as

$$\gamma = \frac{\sqrt{2}}{3p_{\mathrm{a}}^2 \cdot \left(\frac{3}{p_{\mathrm{a}}}\right)^g \sqrt{\frac{p'^{2g}_{\mathrm{TC}}}{q^4_{\mathrm{TC}}} + \frac{p'^{2g}_{\mathrm{TE}}}{q^4_{\mathrm{TE}}}}} \tag{33}$$

When $\beta = 0$, the trace of the surface on the octahedral plane is circular. Hence the surface becomes Lode angle independent. In this case γ can be derived from Eq. (30) as

$$\gamma = \frac{q^2_{\mathrm{TC}}}{3p^2_{\mathrm{a}}} \cdot \left(\frac{p_{\mathrm{a}}}{3p'_{\mathrm{TC}}}\right)^g \tag{34}$$

Parameter R represents the material triaxial strength in tension. It denotes the distance from the origin of the intersection of the ultimate surface with the p' axis (see Fig. 5(a)). R can be determined by

$$R = \frac{c^{2/g}(1-\beta)^{1/2g}}{\sqrt[g]{3\gamma} \cdot p_{\mathrm{a}}^{(2/g-1)}} \tag{35}$$

where c is the intercept along the q axis at $p' = 0$ and it represents the cohesive strength of the material.

4.2. State change parameter *n*

Parameter n is related to the state of stress at which the volumetric response changes from compaction to dilation. It is related to the apex point on the yield surface (Fig. 5(a)), where $\partial F/\partial I_1 = 0$. This condition leads to

$$\frac{\partial F}{\partial I_1} = \frac{1}{p_{\mathrm{a}}} \cdot \left[\alpha \cdot n \cdot \left(\frac{I_1 + R}{p_{\mathrm{a}}}\right)^{n-1} - \gamma \cdot g \cdot \left(\frac{I_1 + R}{p_{\mathrm{a}}}\right)^{g-1}\right] (1 - \beta \cdot \cos 3\theta)^{-1/2} = 0 \tag{36}$$

Hence

$$\frac{\gamma \cdot g}{\alpha n} = \left(\frac{I_1 + R}{P_\mathrm{a}}\right)^{n-g} \tag{37}$$

The modified yield function Eq. (5) can be rewritten as

$$\frac{J_2}{P_\mathrm{a}^2} - \left\{\left(\frac{I_1 + R}{P_\mathrm{a}}\right)^{g} \cdot \left[-\alpha \cdot \left(\frac{I_1 + R}{P_\mathrm{a}}\right)^{n-g} + \gamma\right]\right\} \cdot (1 - \beta \cdot \cos 3\theta)^{-1/2} = 0 \tag{38}$$

Substituting Eq. (37) into Eq. (38) results

$$\frac{J_2}{P_\mathrm{a}^2} - \left\{\left(\frac{I_1 + R}{P_\mathrm{a}}\right)^{g} \cdot \gamma\left(1 - \frac{g}{n}\right)\right\} \cdot (1 - \beta \cdot \cos 3\theta)^{-1/2} = 0 \tag{39}$$

Therefore, n in Eq. (39) can be expressed as

$$n = \frac{g}{1 - \frac{J_2}{\left(\frac{I_1 + R}{p_\mathrm{a}}\right)^{g} \cdot \gamma \cdot p_\mathrm{a}^2 \cdot (1 - \beta \cdot \cos 3\theta)^{-1/2}}} \tag{40}$$

Eq. (40) can also be written in terms of deviator stress q and effective stress p' as

$$n = \frac{g}{1 - \frac{q^2}{3\gamma \cdot (3p')^{g} \cdot p_\mathrm{a}^{2-g} (1 - \beta \cdot \cos 3\theta)^{-1/2}}} \tag{41}$$

According to the discussion in Section 2, dense and loose sands or overconsolidated and normally consolidated clays have different dilation behaviour. It can be assumed that the characteristic state of dense sand or the ultimate stress state of loose sand is associated with the moment when the soil begins to dilate, Fig. 6.

From experimental results, the values of the deviator stress q and the effective stress p' can be measured at points of material volumetric change. Hence, by substitution of these values into Eq. (41), parameter n can be obtained.

4.3. Parameter α for material hardening simulation

As indicated in the foregoing section, the model hardening parameter α in Eq. (16) is influenced by the coupled action of volumetric and deviatoric plastic deformations. It may be expressed in terms of volumetric and deviatoric hardening components α_v and α_d respectively. a_1, b_1, c_1, and d_1 are the hardening parameters required to be determined. The individual expressions of these parameters can be determined by standard laboratory tests.

4.3.1. Determination of a_1 and b_1

The volumetric hardening function α_v and its corresponding parameters a_1 and b_1 can be determined on the basis of exclusively isotropic compression stress paths.

In Fig. 11(a), the yield surfaces of a soil material at two states of stress are plotted in the $p' : q$ space. The isotropic compression stress states are located at the tip of the yield surface e.g. points A and B. [2] Points A and B are also plotted on the compression plane, Fig. 11(b). On this plane, a change in p' from A to B, leads to a change in volume. From Fig. 11(b), the plastic irrecoverable change of specific volume v between compression state p'_A and p'_B can be expressed as

---

[2] As shown in Fig. 11(a), an important characteristic of the yield surface is that it intersects the compressive p' axis at right angles.

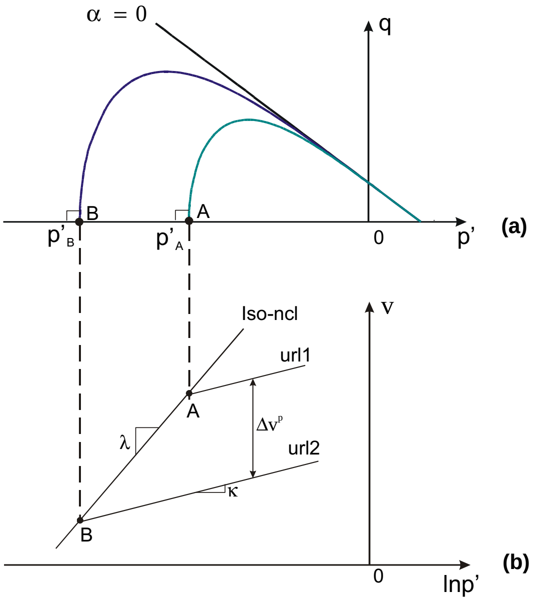

Fig. 11. Successive yield surfaces, isotropic normal compression line (iso-ncl) and unloading–reloading line (url) in compression plane resulting from isotropic normal compression.

$$\Delta v^{\mathrm{p}} = \lambda \cdot \ln\left(\frac{p'_{\mathrm{B}}}{p'_{\mathrm{A}}}\right) - \kappa \cdot \ln\left(\frac{p'_{\mathrm{B}}}{p'_{\mathrm{A}}}\right) \tag{42}$$

where the first term of Eq. (42) represents the total volume change occurring as p' is increased from A to B, and the second term is the elastic recoverable volume change when p' is reduced. The superscript p in the above equation denotes a plastic component.

Furthermore, Eq. (42) can be rearranged as

$$\Delta v^{\mathrm{p}} = (\lambda - \kappa) \cdot \ln\left(\frac{p'_{\mathrm{B}}}{p'_{\mathrm{A}}}\right) \tag{43}$$

In differential form Eq. (43) can be written in generalized form as

$$\mathrm{d}v^{\mathrm{p}} = (\lambda - \kappa) \cdot \frac{\mathrm{d}p'_0}{p'_0} \tag{44}$$

where p'_0 represents the mean effective stress at the tip of the yield surface during material isotropic compression.

The incremental specific volume $\mathrm{d}v^{\mathrm{p}}$ produces incremental plastic volumetric strain:

$$\mathrm{d}\varepsilon_{\mathrm{v}}^{\mathrm{p}} = \frac{\mathrm{d}v^{\mathrm{p}}}{v} \tag{45}$$

Substituting $\mathrm{d}v^{\mathrm{p}}$ from Eq. (44), the incremental plastic volumetric strain in Eq. (45) can be rewritten as

$$\mathrm{d}\varepsilon_{\mathrm{v}}^{\mathrm{p}} = (\lambda - \kappa) \cdot \frac{\mathrm{d}p'_0}{v \cdot p'_0} = \frac{\lambda - \kappa}{1 + e} \cdot \frac{\mathrm{d}p'_0}{p'_0} \tag{46}$$

where e is the void ratio of the material at p'_0.

By integrating Eq. (46) from p'_{A} to p'_{B}, the corresponding plastic volumetric strain can be obtained as

$$\varepsilon_{\mathrm{v}}^{\mathrm{p}} = \frac{\lambda - \kappa}{1 + e} \cdot \int_{p'_{\mathrm{A}}}^{p'_{\mathrm{B}}} \frac{\mathrm{d}p'_0}{p'_0} = \frac{\lambda - \kappa}{1 + e} \cdot \ln \frac{p'_{\mathrm{B}}}{p'_{\mathrm{A}}} \tag{47}$$

Hence, the mean effective stress p'_{B} in Eq. (47) can be expressed as

$$p'_{\mathrm{B}} = p'_{\mathrm{A}} \cdot \mathrm{e}^{\left(\frac{1+e}{\lambda-\kappa}\right)} \cdot \varepsilon_{\mathrm{v}}^{\mathrm{p}} \tag{48}$$

Since p'_{B} is at the intersection of the yield surface with the hydrostatic axis p', it can also be obtained by setting $q = 0$ in the yield function, hence:

$$p'_{\mathrm{B}} = \frac{p_{\mathrm{a}}}{3} \cdot \left(\frac{\alpha_{\mathrm{v}}}{\gamma}\right)^{\frac{1}{g-n}}. \tag{49}$$

Substituting Eq. (49) into Eq. (48), the volumetric hardening function α_{v} can be derived as

$$\alpha_{\mathrm{v}} = \gamma \cdot \left(\frac{3p'_{\mathrm{A}}}{p_{\mathrm{a}}}\right)^{(g-n)} \cdot \mathrm{e}^{\frac{(1+e)(g-n)}{\lambda-k} \cdot \varepsilon_{\mathrm{v}}^{\mathrm{p}}} \tag{50}$$

Assuming $p'_{\mathrm{A}} = p_{\mathrm{c}}$ where p_{c} is the soil pre-consolidation pressure and considering the definition of effective volumetric plastic strain ξ_{v} in Eq. (14), α_{v} in Eq. (50) can be written as

$$\alpha_{\mathrm{v}} = \gamma \cdot \left(\frac{3p_{\mathrm{c}}}{p_{\mathrm{a}}}\right)^{(g-n)} \cdot \mathrm{e}^{\frac{\sqrt{3} \cdot (1+e_0)(g-n)}{\lambda-k} \cdot \xi_{\mathrm{v}}} \tag{51}$$

where e_0 is the void ratio at p_{c}.

Hence, parameters a_1 and b_1 in Eq. (17) can be expressed as

$$a_1 = \gamma \cdot \left(\frac{3p_{\mathrm{c}}}{p_{\mathrm{a}}}\right)^{(g-n)} \tag{52}$$

$$b_1 = \frac{\sqrt{3} \cdot (1 + e_0)(g - n)}{\lambda - k} \tag{53}$$

Apparently, all quantities in Eq. (52) and (53) can be determined easily by standard soil triaxial tests.

4.3.2. Determination of c_1 and d_1

In a CTC test for sand, the relationship between the plastic shear strain and the effective stress ratio can be formulated as a hyperbolic function (Duncan and Chang, 1970; Vermeer, 1980):

$$\varepsilon_1^{\mathrm{p}} - \varepsilon_2^{\mathrm{p}} = \left(\frac{p'}{p_{\mathrm{a}}}\right)^{h_1} \cdot h_2 \cdot \left(\frac{q/p'}{M' - q/p'}\right) \tag{54}$$

where $\varepsilon_1^{\mathrm{p}}$ and $\varepsilon_2^{\mathrm{p}}$ stand for the principle plastic strains, $M' = \sqrt{27\gamma}$ is the peak stress ratio and h_1, h_2 are material constants which can be obtained by comparing the results of the tests with different confining pressures. On a physical basis, these two constants correspond to the index of pressure sensitivity and plastic flow with respect to shear strain hardening behaviour.

According to Eq. (13), the total deviatoric effective plastic strain ξ_{d} can be written as

$$\xi_{\mathrm{d}} = \sqrt{\frac{2}{3}} \cdot (\varepsilon_1^{\mathrm{p}} - \varepsilon_2^{\mathrm{p}}) \tag{55}$$

Substituting Eq. (55) into Eq. (54), the deviatoric effective plastic strain ξ_{d} can be expressed in terms of the effective stress ratio q/p' as

$$\xi_{\mathrm{d}} = \sqrt{\frac{2}{3}} \cdot \left(\frac{p'}{p_{\mathrm{a}}}\right)^{h_1} \cdot h_2 \cdot \left(\frac{q/p'}{M' - q/p'}\right) \tag{56}$$

By assuming $p' = p_{\mathrm{c}}$, where p_{c} is the soil pre-consolidation pressure, the following expression is derived from Eq. (56):

$$\left(\frac{q}{p_{\mathrm{c}}}\right)^2 = \left(\frac{\xi_{\mathrm{d}}}{d_1 + \xi_{\mathrm{d}}}\right)^2 \cdot (M')^2 \tag{57}$$

in which

$$d_1 = \sqrt{\frac{2}{3}} \cdot h_2 \cdot \left(\frac{p_{\mathrm{c}}}{p_{\mathrm{a}}}\right)^{h_1} \tag{58}$$

Furthermore, by rearranging the yield function, the following expression can be obtained:

$$\alpha\left(\frac{3p_{\mathrm{c}}}{p_{\mathrm{a}}}\right)^{n-2} = \gamma\left(\frac{3p_{\mathrm{c}}}{p_{\mathrm{a}}}\right)^{g-2} - \frac{1}{27} \cdot \left(\frac{q}{p_{\mathrm{c}}}\right)^2 \tag{59}$$

Finally, by substituting Eq. (57) into Eq. (59), the expression of deviatoric hardening parameter α_{d} is derived as

$$\alpha_{\mathrm{d}} = c_1 \cdot \left[1 - \frac{(M')^2}{27\gamma}\left(\frac{\xi_{\mathrm{d}}}{d_1 + \xi_{\mathrm{d}}}\right)^2 \left(\frac{3p_{\mathrm{c}}}{p_{\mathrm{a}}}\right)^{2-g}\right] \tag{60}$$

with

$$c_1 = \gamma \cdot \left(\frac{3p_{\mathrm{c}}}{p_{\mathrm{a}}}\right)^{(g-n)} \tag{61}$$

Parameters c_1 in Eq. (61) and d_1 in Eq. (58) can be determined easily on the basis of standard soil triaxial tests. By comparing Eq. (52) and Eq. (61), it can be observed that a_1 and c_1 are identical. Therefore the total material hardening parameters in Eq. (16) are reduced from four to three.

4.4. Parameter α for material softening simulation

As discussed in foregoing section, after a material reaches its ultimate response, softening (degradation) starts.

The softening process can be simulated by specifying the expression of α in the form of a growth function:

$$\alpha = \eta_{\mathrm{s}} \cdot \alpha_{\mathrm{u}} + (1 - \eta_{\mathrm{s}}) \cdot \alpha_{\mathrm{R}} \tag{62}$$

in which

$$\eta_{\mathrm{s}} = \mathrm{e}^{-\kappa_1 \cdot \xi_{\mathrm{pf}}} \tag{63}$$

where α_{u} and α_{R} are the values of α corresponding to material ultimate stress response and material residual stress state respectively, Fig. 12(a). Parameter κ_1 determines the material degradation rate and ξ_{pf} is the post fracture equivalent plastic strain. The value of ξ_{pf} is computed from:

$$\xi_{\mathrm{pf}} = \int \left(\mathrm{d}\varepsilon_{ij}^{\mathrm{p}} \cdot \mathrm{d}\varepsilon_{ij}^{\mathrm{p}}\right)^{1/2} \tag{64}$$

where $\mathrm{d}\varepsilon_{ij}^{\mathrm{p}}$ are the incremental plastic strains measured after material degradation initiation.

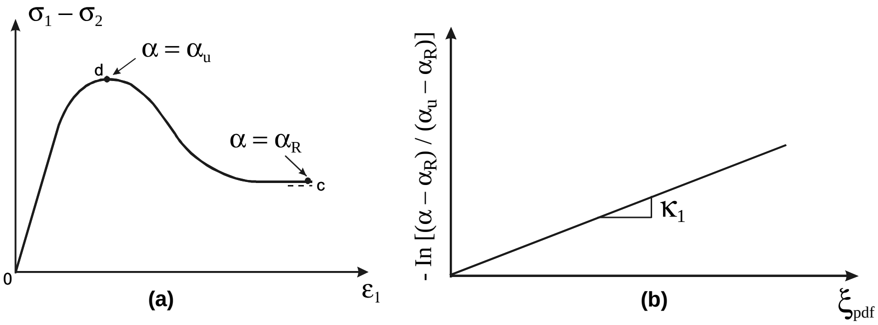

Fig. 12. Determination of softening parameters.

In order to determine parameter κ_1 in Eq. (63), Eq. (62) can be written as

$$\frac{\alpha - \alpha_R}{\alpha_u - \alpha_R} = e^{-\kappa_1 \cdot \xi_{pf}} \tag{65}$$

By taking the logarithm of both sides of Eq. (65), it results:

$$-\ln\left(\frac{\alpha - \alpha_R}{\alpha_u - \alpha_R}\right) = \kappa_1 \cdot \xi_{pf} \tag{66}$$

The plot of $-\ln[(\alpha - \alpha_R)/(\alpha_u - \alpha_R)]$ versus ξ_{pf} provides the value of κ_1 as the slope of the line that intersects the origin of the coordinate system, Fig. 12(b). Hence, from Eq. (66), κ_1:

$$\kappa_1 = -\frac{1}{\xi_{pf}} \cdot \ln\left(\frac{\alpha - \alpha_R}{\alpha_u - \alpha_R}\right) \tag{67}$$

By rearranging the yield function, Eq. (6), the values of both α_R and α_u can be computed by

$$\alpha = \frac{\gamma\left(\frac{3p'}{p_a}\right)^{g-2} - \frac{1}{27} \cdot \left(\frac{q}{p'}\right)^2 \cdot (1 - \beta \cdot \cos 3\theta)^{1/2}}{\left(\frac{3p'}{p_a}\right)^{n-2}} \tag{68}$$

If the material residual stress state coincides with the material critical stress state, the stress ratio in Eq. (68) is typically expressed as $q/p' = M$. Hence α_R in Eq. (68) can be expressed as

$$\alpha_R = \frac{\gamma\left(\frac{3p'}{p_a}\right)^{g-2} - \frac{1}{27} \cdot (M)^2 \cdot (1 - \beta \cdot \cos 3\theta)^{1/2}}{\left(\frac{3p'}{p_a}\right)^{n-2}} \tag{69}$$

When the trace of the surface on the octahedral plane is circular, (i.e. $\beta = 0$), the simplified form of α_R is:

$$\alpha_R = \frac{\gamma\left(\frac{3p'}{p_a}\right)^{g-2} - \frac{1}{27} \cdot (M)^2}{\left(\frac{3p'}{p_a}\right)^{n-2}} \tag{70}$$

According to the discussion in the foregoing section, when $\alpha = 0$, intersection of the yield surface with the hydrostatic axis p' is at negative infinity. This represents the ultimate yielding of a material point associating α_u with $\alpha = 0$.

By means of Eq. (69)or Eq. (70), parameter κ_1 in Eq. (67) can be determined experimentally on the basis of the response degradation stress strain curve.

4.5. Nonassociative parameter κ_c

In the case of nonassociated plasticity, the plastic potential function Q is expressed as

$$Q = \frac{J_2}{p_a^2} - \left[-\alpha_Q \cdot \left(\frac{I_1 + R}{p_a} \right)^n + \gamma \cdot \left(\frac{I_1 + R}{p_a} \right)^g \right] \cdot F_s \tag{71}$$

where F_s is defined in Eq. (2) and

$$\alpha_Q = \alpha + \kappa_c(\alpha_0 - \alpha)(1 - \chi_v) \tag{72}$$

On the basis of the procedures described by Frantziskonis et al. (1986), the nonassociative parameter κ_c is determined as follows.

According to the flow rule, the incremental plastic strain $d\varepsilon_{ij}^p$ is given as

$$d\varepsilon_{ij}^p = d\lambda \cdot \frac{\partial Q}{\partial \sigma_{ij}} \tag{73}$$

Therefore, the corresponding incremental forms of the volumetric plastic strain $d\varepsilon_v^p$ and one of the principle plastic strains $d\varepsilon_{11}^p$ can be written as

$$d\varepsilon_v^p = 3d\lambda \cdot \frac{\partial Q}{\partial I_1} \tag{74}$$

$$d\varepsilon_{11}^p = d\lambda \cdot \frac{\partial Q}{\partial \sigma_{11}} \tag{75}$$

The ratio of Eqs. (74) and (75) yields:

$$\vartheta = \frac{d\varepsilon_v^p}{d\varepsilon_{11}^p} = \frac{3\frac{\partial Q}{\partial I_1}}{\frac{\partial Q}{\partial \sigma_{11}}} \tag{76}$$

ϑ can be obtained from a shear test as the slope of the observed ε_v^p versus ε_1^p response at peak, e.g. point d in Fig. 13(b).

The derivatives of the plastic potential Q in Eq. (71) with respect to the principal stress σ_{11} and the stress invariant I_1 are:

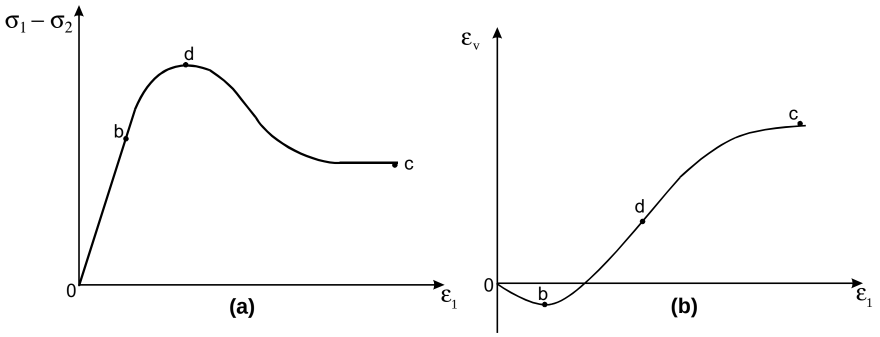

Fig. 13. Schematic of soil shear stress and volumetric strain versus axial strain.

$$\frac{\partial Q}{\partial \sigma_{11}} = \frac{\partial Q}{\partial I_1} + \frac{\partial Q}{\partial J_2} \cdot s_{11} + \frac{\partial Q}{\partial J_3} \cdot \left(s_{lk} \cdot s_{kl} - \frac{2}{3} \cdot J_2 \right) \tag{77}$$

$$\frac{\partial Q}{\partial I_1} = -\frac{1}{p_\mathrm{a}} \left[-\alpha_Q \cdot n \cdot \left(\frac{I_1 + R}{p_\mathrm{a}} \right)^{n-1} + \gamma \cdot g \cdot \left(\frac{I_1 + R}{p_\mathrm{a}} \right)^{g-1} \right] \cdot F_\mathrm{s} \tag{78}$$

in which $s_{ij} = \sigma_{ij} - 1/3 \cdot I_1 \cdot \delta_{ij}$ and δ_{ij} is the Kronecker delta.

Substitution of Eqs. (77) and (78) into Eq. (76) leads to:

$$3 \cdot \frac{\partial Q}{\partial I_1} = \vartheta \cdot \left[\frac{\partial Q}{\partial I_1} + \frac{\partial Q}{\partial J_2} \cdot s_{11} + \frac{\partial Q}{\partial J_3} \cdot \left(s_{lk} \cdot s_{kl} - \frac{2}{3} \cdot J_2 \right) \right] \tag{79}$$

The plastic potential Q in Eq. (71) can be also expressed as

$$Q = F + \alpha_Q \cdot \left(\frac{I_1 + R}{p_\mathrm{a}} \right)^n \cdot F_\mathrm{s} \tag{80}$$

with $F = \frac{J_2}{p_\mathrm{a}^2} - \gamma \cdot \left(\frac{I_1 + R}{p_\mathrm{a}} \right)^g \cdot F_\mathrm{s}$.

Substituting Eq. (80) into Eq. (79) leads to:

$$\begin{aligned} &\alpha_Q \cdot \left[(3 - \vartheta) \cdot \frac{n}{p_\mathrm{a}} \cdot F_\mathrm{s} \cdot \left(\frac{I_1 + R}{p_\mathrm{a}} \right)^{n-1} - \vartheta \cdot \left(\frac{I_1 + R}{p_\mathrm{a}} \right)^n \cdot s_{11} \cdot \frac{\partial F_\mathrm{s}}{\partial J_2} - \vartheta \cdot \left(\frac{I_1 + R}{p_\mathrm{a}} \right)^n \cdot \left(s_{lk} \cdot s_{kl} - \frac{2}{3} \cdot J_2 \right) \cdot \frac{\partial F_\mathrm{s}}{\partial J_3} \right] \\ &\quad = \vartheta \cdot s_{11} \cdot \frac{\partial F}{\partial J_2} + \vartheta \cdot \left(s_{lk} \cdot s_{kl} - \frac{2}{3} \cdot J_2 \right) \cdot \frac{\partial F}{\partial J_3} - (3 - \vartheta) \cdot \frac{\partial F}{\partial I_1} \end{aligned} \tag{81}$$

Assuming

$$\overline{X} = (3 - \vartheta) \cdot n \cdot F_\mathrm{s} \cdot \left(\frac{I_1 + R}{p_\mathrm{a}} \right)^{n-1} - \vartheta \cdot \left(\frac{I_1 + R}{p_\mathrm{a}} \right)^n \cdot s_{11} \cdot \frac{\partial F_\mathrm{s}}{\partial J_2} - \vartheta \cdot \left(\frac{I_1 + R}{p_\mathrm{a}} \right)^n \cdot \left(s_{lk} \cdot s_{kl} - \frac{2}{3} \cdot J_2 \right) \cdot \frac{\partial F_\mathrm{s}}{\partial J_3} \tag{82}$$

and

$$\overline{Y} = \vartheta \cdot s_{11} \cdot \frac{\partial F}{\partial J_2} + \vartheta \cdot \left(s_{lk} \cdot s_{kl} - \frac{2}{3} \cdot J_2 \right) \cdot \frac{\partial F}{\partial J_3} - (3 - \vartheta) \cdot \frac{\partial F}{\partial I_1} \tag{83}$$

in which

$$\frac{\partial F_\mathrm{s}}{\partial J_2} = \frac{\partial}{\partial J_2} \left(1 - \frac{3\sqrt{3}}{2} \beta \cdot J_3 \cdot J_2^{-\frac{3}{2}} \right)^{-\frac{1}{2}} = -\frac{9\sqrt{3}}{8} \beta \cdot J_3 \cdot J_2^{-\frac{5}{2}} \cdot \left(1 - \frac{3\sqrt{3}}{2} \beta \cdot J_3 \cdot J_2^{-\frac{3}{2}} \right)^{-\frac{3}{2}} \tag{84}$$

$$\frac{\partial F_\mathrm{s}}{\partial J_3} = \frac{\partial}{\partial J_3} \left(1 - \frac{3\sqrt{3}}{2} \beta \cdot J_3 \cdot J_2^{-\frac{3}{2}} \right)^{-\frac{1}{2}} = \frac{3\sqrt{3}}{4} \beta \cdot J_2^{-\frac{3}{2}} \cdot \left(1 - \frac{3\sqrt{3}}{2} \beta \cdot J_3 \cdot J_2^{-\frac{3}{2}} \right)^{-\frac{3}{2}} \tag{85}$$

$$\frac{\partial F}{\partial I_1} = -\frac{\gamma g}{p_\mathrm{a}} \cdot \left(\frac{I_1 + R}{p_a} \right)^{g-1} \cdot F_s \tag{86}$$

$$\frac{\partial F}{\partial J_2} = \frac{1}{p_a^2} - \gamma \cdot \left(\frac{I_1 + R}{p_\mathrm{a}}\right)^g \cdot \frac{\partial F_\mathrm{s}}{\partial J_2} \tag{87}$$

$$\frac{\partial F}{\partial J_3} = -\gamma \cdot \left(\frac{I_1 + R}{p_a}\right)^g \cdot \frac{\partial F_s}{\partial J_3} \tag{88}$$

Therefore Eq. (81) can be written as

$$\alpha_Q = \frac{\overline{Y}}{\overline{X}} \tag{89}$$

By substitution of Eq. (89) into Eq. (72), the parameter κ_c related to the nonassociative behaviour can be determined as

$$\kappa_\mathrm{c} = \frac{\alpha_Q - \alpha}{(\alpha_0 - \alpha) \cdot (1 - \chi_\mathrm{v})} \tag{90}$$

Experimentally κ_c can be determined by utilizing a number of tests along different stress paths.

5. Model verification

5.1. Test material and test method

In order to verify the proposed constitutive model, Eastern Scheldt sand was chosen as the test material. This sand is obtained from Eastern Scheldt in the Netherlands, which consists of 95% quartz and 5% glauconite. The shape of the grains of the sand can be characterized as subrounded. The classification properties of Eastern Scheldt sand are summarized in Table 1 (Cheng et al., 2001).

In this study, Eastern Scheldt sand was chosen as the test material because several dams have been constructed in the recent past in the Eastern Scheldt region of the Netherlands for reasons of environmental protection, safety and water control. In each of these dams, at three locations, closure gaps were constructed, that were finally closed by sand. Therefore, the investigation of the mechanical response of this type of sand and its failure response became of importance.

The tests were carried out in the laboratory of GeoDelft by using the triaxial test apparatus shown in Fig. 14 and reported in Cheng et al. (2001). Measurements of axial load, axial displacement, cell pressure and volume change were collected and processed.

The tests were performed on medium dense and dense sand specimens with relative densities of $D_\mathrm{r} = 0.4$ and 0.7 respectively. The medium dense sand specimens (MF series) were prepared in a cylindrical split mould by air pluviation with average initial void ratio of $e_0 = 0.725$. The dense sand specimens (DF series) were prepared in the same type of mould by the multi-stages vibration method with average initial void ratio of $e_0 = 0.625$. Both of the preparation methods achieved very reproducible densities.

The specimen was encased by a flexible membrane and two end caps. Thus the confining fluid did not penetrate the pore space. In order to keep the homogeneity of the specimen during testing, lubricated ends

Table 1
Classification properties for Eastern Scheldt sand

Properties	Values	Properties	Values
Specific gravity, G_s	2.65	Mean grain size, D_{50}	0.156 mm
Max. void ratio, e_max	0.859	D_{60}	0.17 mm
Min. void ratio, e_min	0.528	Uniformity coefficient, D_{60}/D_{10}	1.7

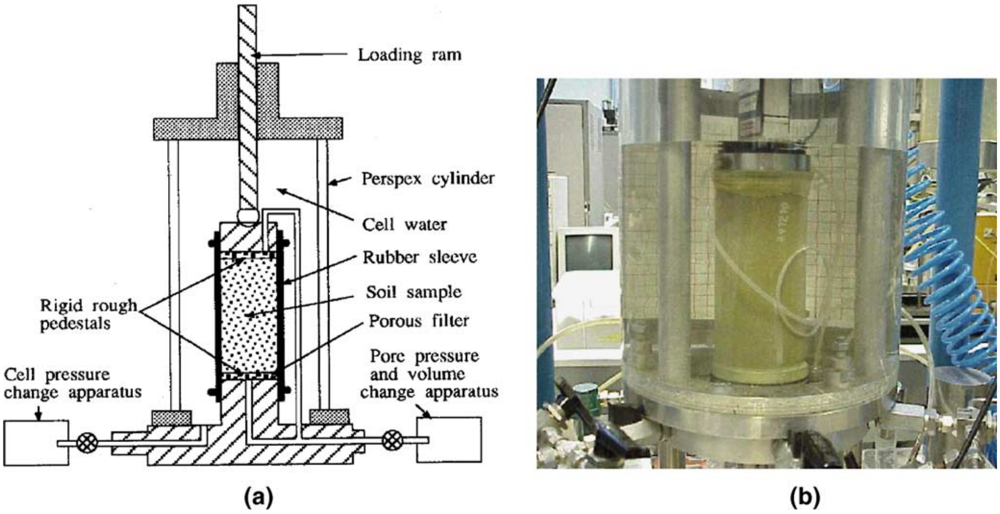

Fig. 14. Triaxial test apparatus. (a) details of the device; (b) laboratory test setup.

were used to minimize end restraint effects. The lubrication layer is composed of a layer of grease (30–50 μm) and a latex disk (200 μm).

During the tests, the axial force and displacement were measured, as well as the cell pressure and the pore water pressure. Before starting the shear loading, the saturated specimen was first consolidated isotropically at a loading rate of 3 kPa per minute. Afterwards, the specimen was sheared at a constant axial strain rate 3% per hour for conventional compression tests and at a constant axial stress rate of 3 kPa per minute for stress control tests.

All the specimens were sheared into the softening region. Unloading and reloading stress paths with a stress rate of 10 kPa per minute were imposed on some dense sand specimens during consolidation and shearing tests. Additionally three quick loading tests with strain rate of 0.4% per minute (strain controlled) and 12 kPa per minute (stress controlled) were carried out for studying the influence of loading rate on material characteristic states.

Cylindrical specimens were utilized with a height and diameter of approximately 66 mm. A few specimens with a slenderness ratio of 2 were tested for reference. During the consolidation and shearing process, the specimen was fully drained (open valves).

In order to investigate the influence of initial conditions and of the stress path on the material parameters, two initial consolidation pressures (150 and 400 kPa) and three different stress paths, i.e. CTC, TC and RTC, Fig. 15, are investigated experimentally.

This stress path is perpendicular to the p' axis. Since these three stress paths include most of the main loading directions in the compression space, they are sufficient to characterize the compression behaviour of the material. Table 2 lists all test series numbers with the corresponding stress paths and the initial consolidation pressures. These series numbers will be utilized in the next section to indicate corresponding tests.

5.2. Material parameters evaluation for eastern Scheldt sand

Table 3 summarizes the test results conducted along three stress paths at peak response and characteristic state. Details of the experimental results can be found in the report by Cheng et al. (2001).

As expected, in Table 3, sands tested at a lower relative density (MF test series) but with the same confinement, exhibit lower ultimate strength than those at higher relative density (DF test series). It is also

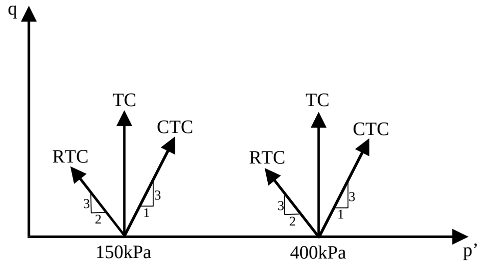

Fig. 15. Stress paths and stress level plotted in $p' - q$ stress space.

Table 2
List of stress paths and test series numbers

Type of sand		Medium dense			Dense		
Stress path		CTC	RTC	TC	CTC	RTC	TC
Initial confining pressure (kPa)	150	MF1	MF3	MF5	DF1	DF2	DF3
	400	MF2	MF4	MF6	DF4	DF5	DF6

Table 3
Results at peak response and characteristic state of Eastern Scheldt sand

Stress path	Test no.	q_{ul} (kPa)	p'_{ul} (kPa)	M'	ϕ_{ul}	q_{cl} (kPa)	p'_{cl} (kPa)	M	ϕ_{cl}
CTC	MF1	401.86	283	1.42	35.0	343	263	1.30	32.3
	MF2	1080.6	761	1.42	35.0	919	706	1.30	32.3
	DF1	513	317	1.62	35.7	322	253	1.27	31.6
	DF4	1197	801	1.5	36.8	801	668	1.20	30.0
TC	MF5	240.25	155	1.55	38.0	207	154	1.34	33.2
	MF6	–	–	–	–	505	406	1.29	32.1
	DF3	273	154	1.79	37.8	194	151	1.29	32.1
	DF6	669	411	1.63	40.0	490	409	1.22	30.5
RTC	MF3	119.14	74	1.61	39.4	98	86	1.14	28.6
	MF4	303	202	1.5	36.8	269	231	1.13	28.4
	DF2	120	65	1.84	44.7	91	84	1.08	27.3
	DF5	348	203	1.72	41.9	277	237	1.17	29.3

observed that medium dense sands dilate at a higher stress level than dense sands. This is because compaction in a loose material continues until no further volume decrease, after which the material begins to dilate. However, for dense materials, dilation initiates from the early stages of shear loading because there is not much void space in the material for compaction.

Fig. 16 shows the experimentally measured state of stress at peak response (filled symbols) and the characteristic state (non-filled symbols) in the $p' - q$ space. A quite pronounced linearity is observed for the characteristic state but not for the ultimate stress state. It can be observed in Fig. 17 that experimentally measured ultimate stress state cannot be represented by a straight line (dash line) but by a curved one (solid line). This means that the constant value of parameter γ in classical yield function cannot be utilized to define the ultimate stress state of the material. It becomes a stress path dependent variable.

In order to make the γ parameter stress path independent we have to change the shape of the yield surface. This can be done by introducing the extra parameter g in the classical formulation, see section

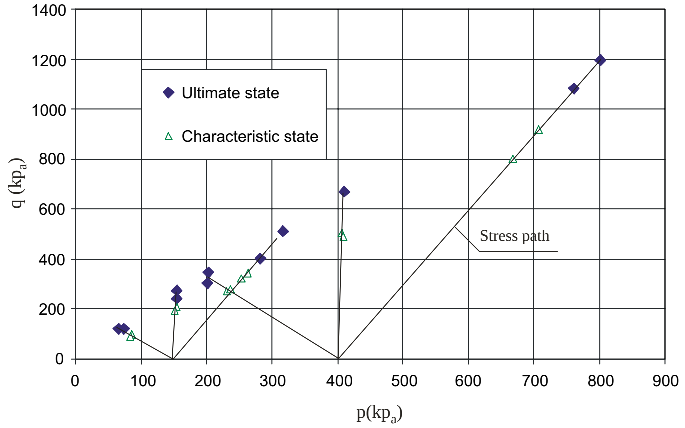

Fig. 16. Ultimate stress state and characteristic stress state for Eastern Scheldt sand.

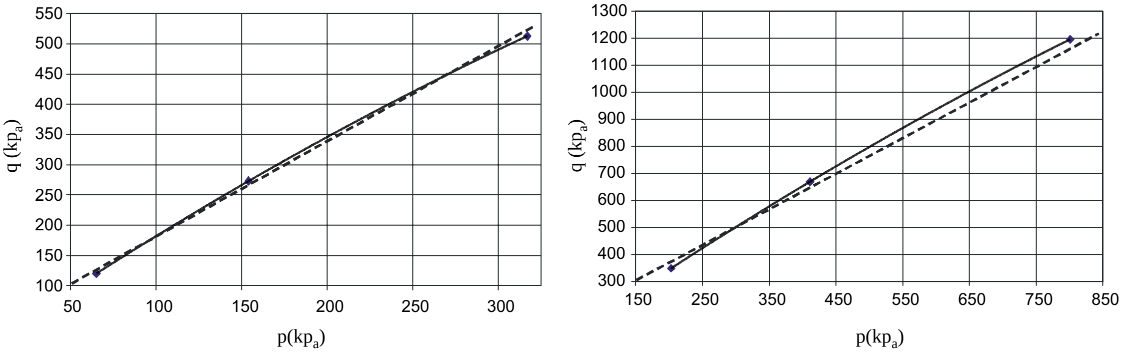

(a) **(b)**

Fig. 17. Experimentally measured ultimate stress state line for Eastern Scheldt sand. (a) $p_c = 150\,\text{kPa}$, DF and (b) $p_c = 400\,\text{kPa}$, DF.

2. In this way, for $g < 2$ the stress response surface has a bigger slope closer to the value $p = 0$, and the slope decreases gradually as p increases. The result of this approach is the fact that under different stress paths the constant value of parameter γ can be utilized for characterizing the ultimate stress state of the same type of sand.

The procedure used for finding the parameter g and the unique value of γ consists of the following. The modified yield function in Eq. (6) at ultimate stage on compressive meridian plane can be written as

$$F = \frac{q^2}{3p_a} - \gamma\left(\frac{3p'}{p_a}\right)^g = 0 \tag{91}$$

The terms of the yield function can be manipulated in order to obtain an equation that can be worked with easier, Eq. (92).

$$q = \sqrt{3p_a^2\gamma\left(\frac{3p'}{p_a}\right)^{g/2}} \tag{92}$$

Also this equation can be written in the form as in Eq. (93).

$$y = a \cdot x^b \tag{93}$$

where

$$a = \sqrt{3p_a^2\gamma}, \quad b = g/2, \quad x = 3p'/p_a. \tag{94}$$

The values of x and y can be obtained from laboratory test data. By using the least square method one can obtain the values of a and b in Eq. (94) and consequently the values of γ and g can be determined by

$$\gamma = \frac{a^2}{3p_a^2}, \quad g = 2b \tag{95}$$

Fig. 18(a) through (d) present the plots in x–y space of the least square method approximations of parameters γ and g.

On the basis of the parameter determination procedure that was presented in the previous section, for some individual tests, the hardening parameters are computed and shown in Table 4.

In Fig. 19, the influence of the material initial relative density on the parameter n is shown. It can first of all be observed that parameter n is indeed influenced by the initial state of the sand and secondly, that lower

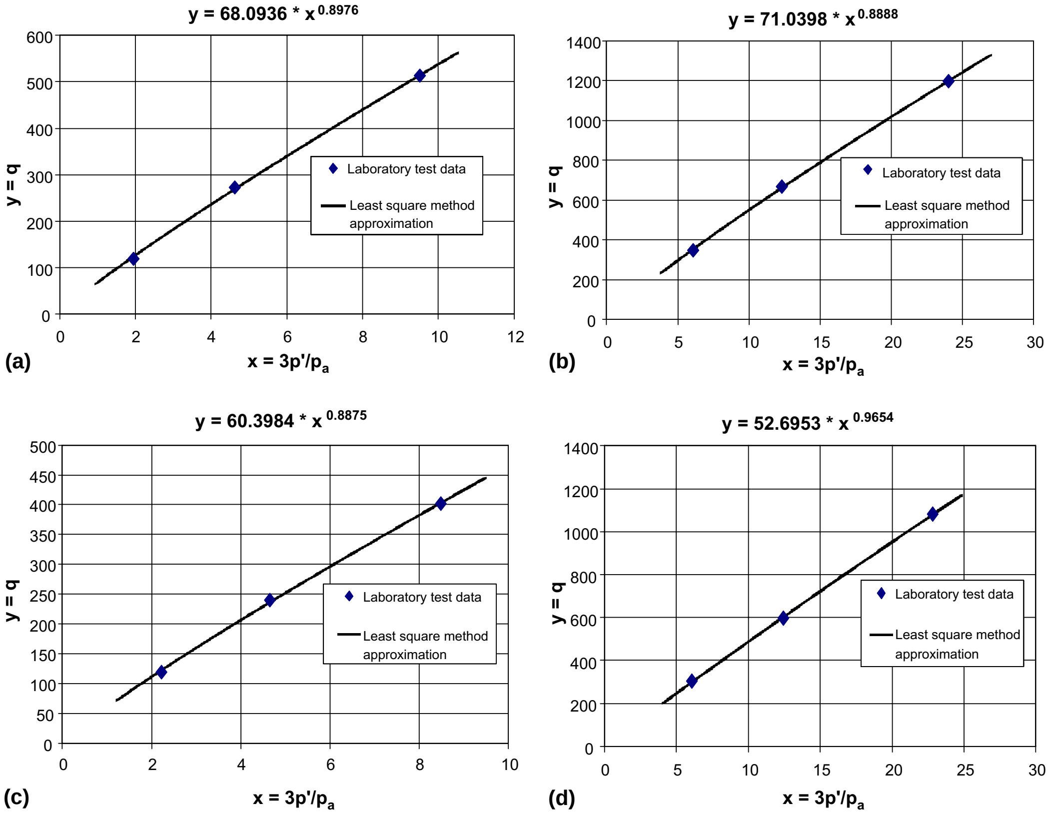

Fig. 18. Least square method approximations of parameters γ and g. (a) $p_c = 150\,\text{kPa}$, DF, (b) $p_c = 400\,\text{kPa}$, DF, (c) $p_c = 150\,\text{kPa}$, MF and (d) $p_c = 400\,\text{kPa}$, MF.

Table 4
Material hardening parameters determined on the basis of different stress path

Stresspath	Test no.	n	g	γ	a_1	b_1	d_1
CTC	MF1	9.49	1.775	0.1215987	1.11E−06	−7683	9.6E−03
	MF2	11.96	1.931	0.0925598	1.397E−12	−9988	8.53E−03
	DF1	5.04	1.795	0.1545582	1.17E−03	−3044	5.53E−03
	DF4	4.48	1.778	0.1682217	2.04E−04	−2534	7.11E−03
TC	MF5	9.49	1.775	0.1215987	1.11E−06	−7683	9.6E−03
	MF6	11.96	1.931	0.0925598	1.397E−12	−9988	8.53E−03
	DF3	5.04	1.795	0.1545582	1.17E−03	−3044	5.53E−03
	DF6	4.48	1.778	0.1682217	2.04E−04	−2534	7.11E−03
RTC	MF3	9.49	1.775	0.1215987	1.11E−06	−7683	9.6E−03
	MF4	11.96	1.931	0.0925598	1.397E−12	−9988	8.53E−03
	DF2	5.04	1.795	0.1545582	1.17E−03	−3044	5.53E−03
	DF5	4.48	1.778	0.1682217	2.04E−04	−2534	7.11E−03

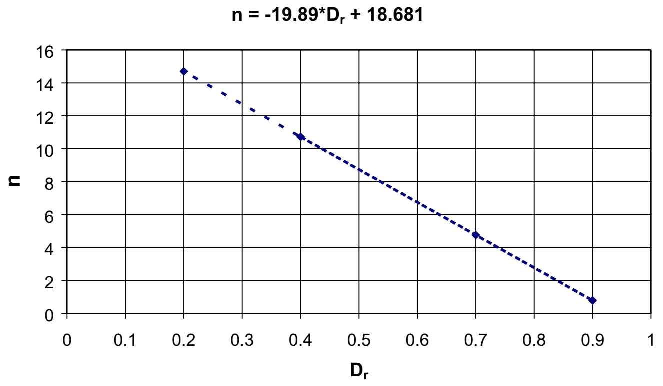

Fig. 19. Plot of n versus D_r.

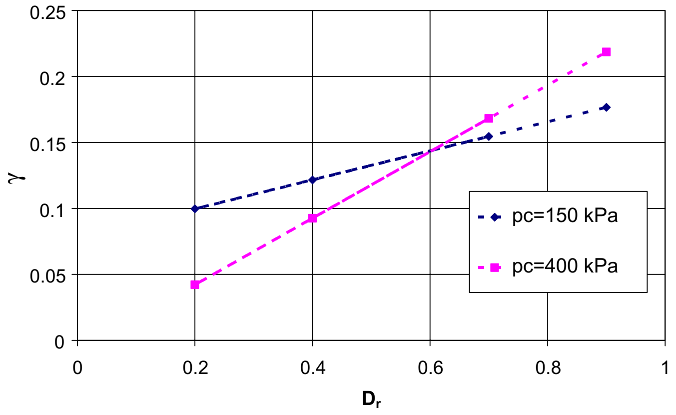

Fig. 20. Plot of γ versus D_r.

values of n result for increasing values of D_r. Since the yield surface with lower n can produce more plastic dilation, see Fig. 2, hence the dense material exhibits more dilatation response than the lower one.

Similarly, Fig. 20 shows also the influence of the material initial relative density on the value of parameter γ. It can be observed that for both initial confining pressures, 150 and 400 kPa, the parameter γ increases with D_r. For higher initial consolidation pressure the value of γ grows faster than for lower pressures. It can be concluded that the ultimate stress response of the sand is influenced strongly by its initial confining pressure. To properly quantify the influence of the material initial state on the values of n and γ, a more extensive experimental investigation still needs to be done.

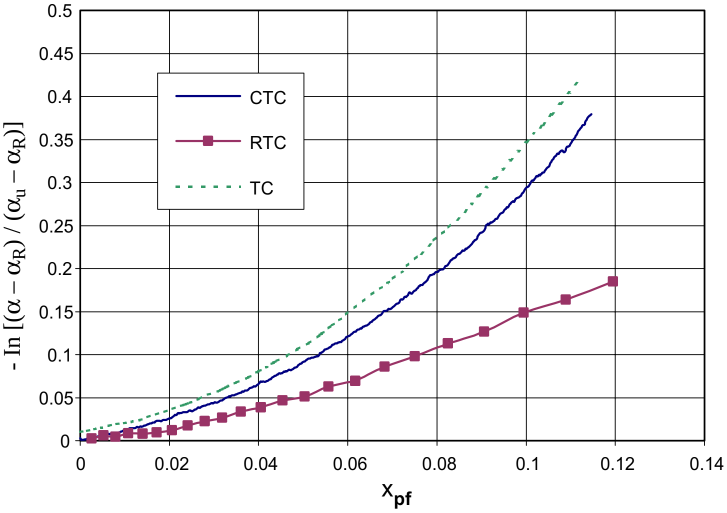

Fig. 21. Plot of $-\ln[(\alpha - \alpha_R)/(\alpha_u - \alpha_R)]$ versus ξ_{pf} to obtain κ_1 for Eastern Scheldt sand ($p_c = 150$ kPa, DF1, DF2, DF3).

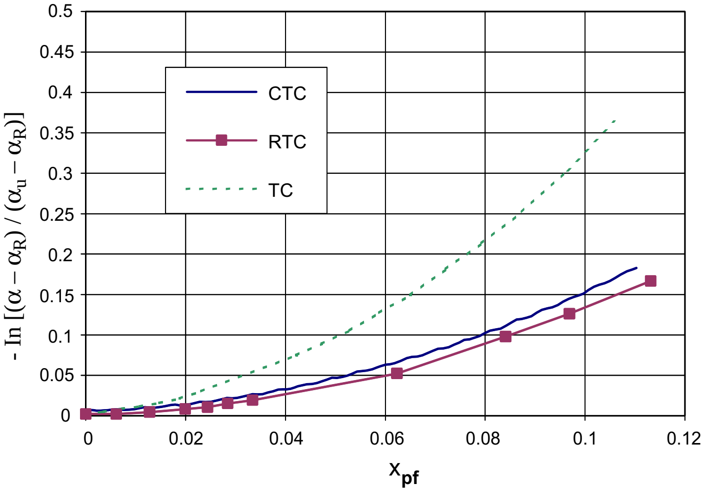

Fig. 22. Plot of $-\ln[(\alpha - \alpha_R)/(\alpha_u - \alpha_R)]$ versus ξ_{pf} to obtain κ_1 for Eastern Scheldt sand ($p_c = 400$ kPa, DF4, DF5, DF6).

In Figs. 21 and 22 the experimentally measured relation between ξ_{pf} and $-\ln[(\alpha - \alpha_R)/(\alpha_u - \alpha_R)]$ is shown for different stress paths and initial levels of confining pressure. From Eq. (67), the average slope of these curves is defined as κ_1. It is observed that sand loaded along a TC stress path exhibits a higher degradation rate than sand loaded along the other two stress paths. Furthermore, lower degradation rates always seem to occur along the RTC stress path. Additionally, the degradation rate in a TC test is more pronounced when the specimen is subjected to higher initial confining pressure.

The reason for higher material response degradation along TC stress paths is that along this stress path the material approaches its residual strength quicker. This can also be explained by the characteristics of the constitutive model. As indicated in Fig. 6, the material is more sensitive to deviatoric than volumetric

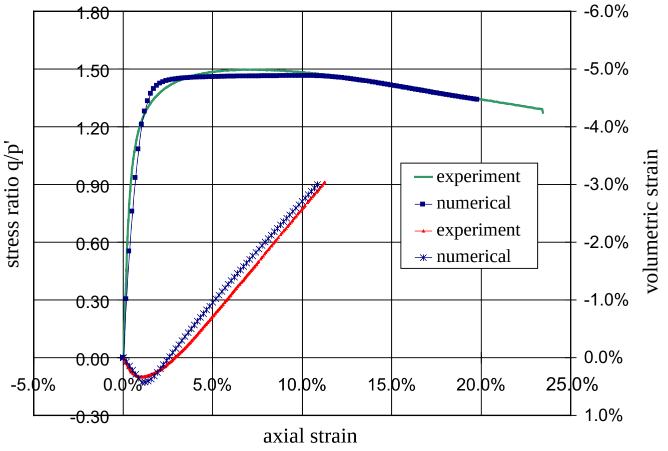

Fig. 23. Comparisons of stress–strain and volumetric response of CTC test with nonassociative flow rules ($p_c = 400$ kPa, DF4).

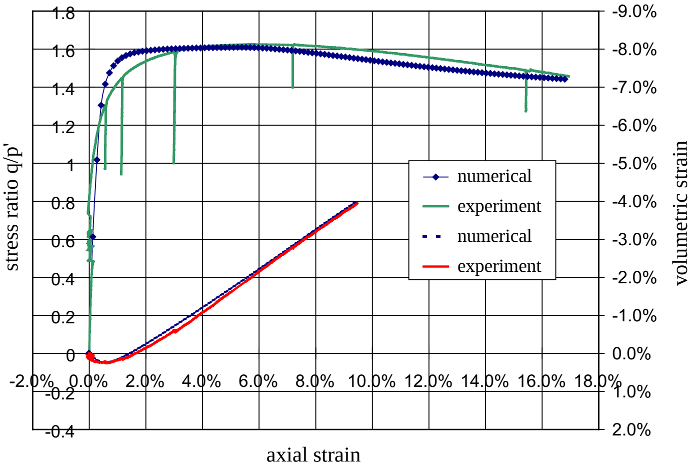

Fig. 24. Comparisons of stress–strain and volumetric response of CTC test with nonassociative flow rule ($p_c = 150$ kPa, F1).

plastic strain components. Along a TC stress path significant deviatoric deformations are produced, leading thus to faster material degradation.

5.3. Numerical predictions and experimental results

Both the capability of the model and the accuracy of the parameter determination of the constitutive model can be examined by comparing the numerical predictions of the material response with the observed laboratory behaviour. Figs. 23–29 present the comparisons of the numerical predictions with the experimental results in terms of stress–strain curves and volumetric response for CTC, TC and RTC tests under different initial confining pressures. The model parameters utilized for each comparison are determined on the basis of the modified form of the yield function.

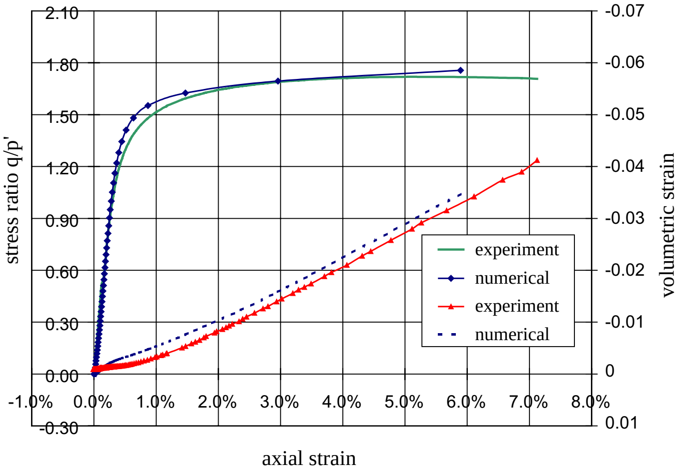

Fig. 25. Comparisons of stress–strain and volumetric response of RTC test with nonassociative flow rule ($p_c = 400\,\text{kPa}$, DF5).

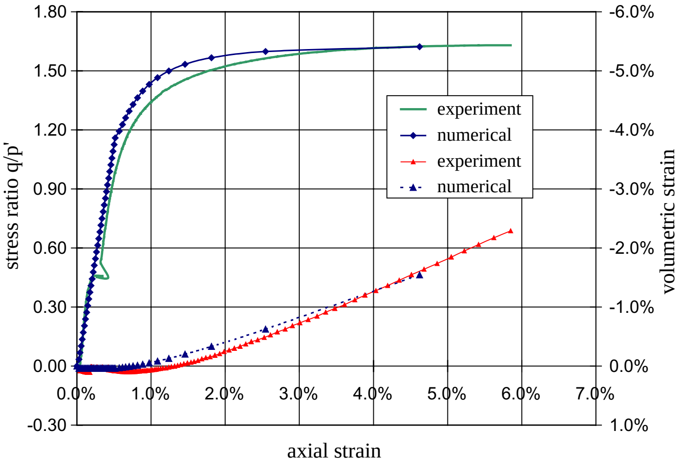

Fig. 26. Comparisons of stress–strain and volumetric response of TC test with nonassociative flow rule ($p_c = 400\,\text{kPa}$, DF6).

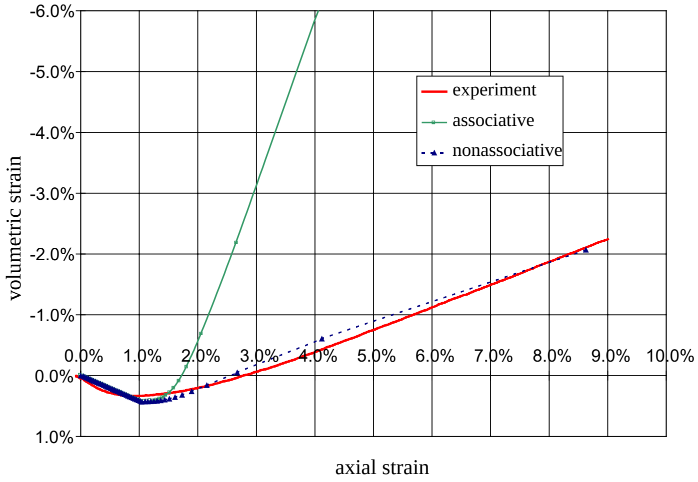

Fig. 27. Comparisons of volumetric response of CTC test with different flow rules ($p_c = 400$ kPa, DF4).

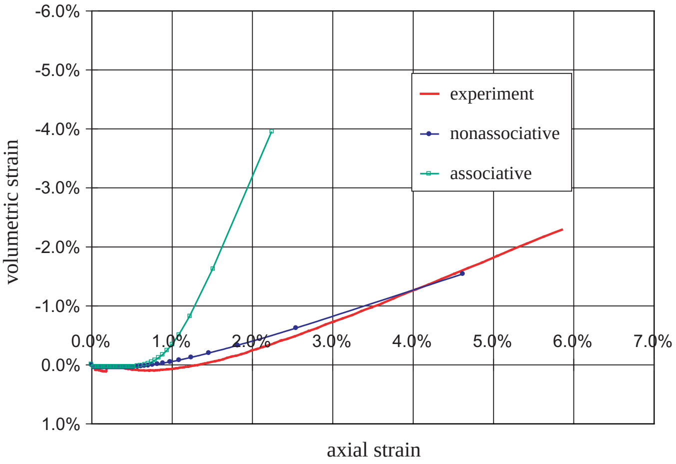

Fig. 28. Comparisons of volumetric response of RTC testwith different flow rules ($p_c = 400$ kPa, DF5).

It is observed that the numerical predictions obtained from the constitutive model show good agreement with the experimental results, Figs. 23–26.

The plots of the volumetric response calculated with different flow rules, Fig. 27–29, show that the model based on the associative plasticity does not show good comparison with the actual observed behaviour. By utilizing an associative flow rule, the model produces an overestimation of the plastic volume strain, especially at stress levels close to the ultimate stress state where excessive dilation can be observed. By correcting the yield function to account for nonassociative plasticity, the model shows good comparison with the observed behaviour in terms of both, stress–strain and volumetric response.

It can be concluded that the nonassociative model is more appropriate for description of the actual material behaviour. The numerical results indicate that, once the appropriate material parameters are available, the model is capable of describing the material response along various stress paths in both the hardening and the softening regimes.

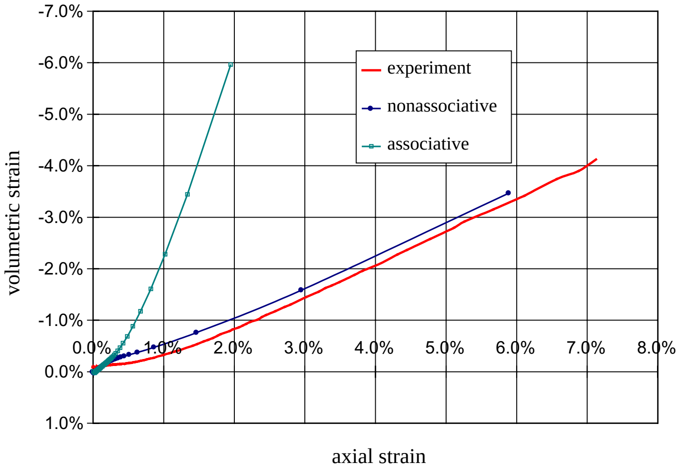

Fig. 29. Comparisons of volumetric response of TC test with different flow rules ($p_0 = 400\,\text{kPa}$, DF6).

6. Conclusions

In this contribution, on the basis of the hierarchical approach, a constitutive model for the soil response in the elastoplastic range has been developed.

The following conclusions may be drawn:

1. The constitutive model is capable of simulating the mechanical characteristics of the material under different stress paths. Utilization of a nonlinear ultimate response surface proved to be a key element in ensuring stress path independency.
2. The hardening parameters employed for isotropic hardening response have been defined as a function of the deformation history. Both volumetric and deviatoric hardening components have been introduced explicitly into the material hardening simulation. An isotropic measure of response flow surface degradation has been introduced into the model to simulate material softening (degradation) by means of specifying parameter α, after response degradation initiation, as an increasing function of the equivalent post fracture plastic strain.
3. An important feature of the model is the existence of two stress state lines, i.e. characteristic state line and ultimate state line, which can provide a realistic representation of the mechanical behaviour of geotechnical materials under engineering conditions.
4. The nonassociative model has been established based on a concept in which the potential function is obtained by a correction/modification of the yield function. This method simplifies the determination of the plastic potential function and it introduces only one extra parameter to account for the material nonassociative behaviour.
5. The model based on a nonassociative flow rule is more appropriate for description of the actual material behaviour. By correcting the yield function to account for nonassociative plasticity, the model shows good comparison with the observed behaviour both in stress–strain and volumetric response.
6. According to the experimental results, some model parameters such as n, γ are the material initial state dependent. However, to quantify properly the influences of the initial state path on these parameters, extensive experimental investigations still need to be done.

The experimental study described in this contribution is a preliminary study. It presents possible directions for further computational and experimental research.

References

Baladi, G.Y., Rohani, B., 1979. Elastic–plastic model for saturated sand. Journal of Geotechnical Engineering Division, ASCE 105 (GT4), 465–480.

Cheng, X., den Haan, E.J., Barends, F.B.J., 2001. Laboratory and Numerical Investigations of Triaxial Compression Behaviour of a Duch Sand. GeoDelft Internal Report.

Davis, E.H., 1968. Theories of plasticity and the failure of soil masses. In: Lee, I.K. (Ed.), Soil Mechanics: Selected Topics. Butterworths, London, pp. 341–380.

Desai, C.S., 1980. A general basis for yield, failure and potential functions in plasticity. International Journal for Numerical and Analytical Methods in Geomechanics 4, 361–375.

Desai, C.S., 2001. Mechanics of materials and interface: the disturbed state concept. CRC Press, LLC, New York.

Desai, C.S., Faruque, M.O., 1984. Constitutive model for geologic materials. Journal of Engineering Mechanics Division, ASCE 110, 1391–1408.

Desai, C.S., Somasundaram, S., Frantziskois, G.N., 1986. A Hierarchical approach for constitutive modelling of geologic materials. International Journal for Numerical and Analytical Methods in Geomechanics 10, 225–257.

DiMaggio, F.L., Sandler, I.S., 1971. Material models for granular soils. Journal of Engineering Mechanics Division, ASCE 97 (EM3), 935–950.

Drucker, D.C., 1951. A more fundamental approach to plastic stress–strain relations. In: Proceedings of the First U.S. National. Congress of Applied Mechanics, Chicago, pp. 487–491.

Duncan, J.M., Chang, C.Y., 1970. Non-linear analysis of stress and strain in soils. Journal of the Soil Mechanics and Foundations Division, ASCE 96, 1629–1653.

Frantziskonis, G., Desai, C.S., Somasundaram, S., 1986. Constitutive model for nonassociative behaviour. Journal of Engineering Mechanics, ASCE 112, 932–945.

Ibsen, L.B., Lade, P.V., 1998. The role of the characteristic line in static soil behaviour. In: Adachi, T., Oka, F., Yashima, A. (Eds.), Localization and Bifurcation Theory for Soils and Rocks. Balkema, Rotterdam, pp. 221–230.

Iwan, W.D., 1967. On a class of models for the yielding behavior of continuous and composite systems. Journal of Applied Mechanics 34, 612–617.

Lacy, S.J., Prevost, J.H., 1987. Constitutive model for geomaterials. In: Proceedings of the Second International Conference on Constitutive Laws for Engineering Material. Elsevier, New York, pp. 149–160.

Lade, P.V., 1977. Elasto-plastic stress–strain theory for cohesionless soil with curved yield surfaces. International Journal of Solids and Structures 13, 1019–1035.

Lade, P.V., 1978. Prediction of undrained behaviour of sand. Journal of Geotechnical Engineering Division, ASCE 104 (GT6), 721–735.

Lade, P.V., Duncan, J.M., 1975. Elastoplastic stress–strain theory for cohesionless soil. Journal of Geotechnical Engineering Division, ASCE 101 (GT10), 1037–1053.

Lade, P.V., Nelson, R.B., Ito, Y.M., 1987. Nonassociated flow and stability of granular materials. Journal of Engineering Mechanics, ASCE 113 (9), 1302–1318.

Lade, P.V., Nelson, R.B., Ito, Y.M., 1988. Instability of granular materials with nonassociated flow. Journal of Engineering Mechanics, ASCE 114 (12), 2173–2194.

Luong, M.P., 1982. Stress–strain aspects of cohesionless soils under cyclic and transient loading. In: International Symposium on Soil under Cyclic and Transient Loading. Balkema, Rotterdam, pp. 315–324.

Mróz, Z., 1967. On the description of anisotropic hardening. Journal of the Mechanics and Physics of Solids 15, 163–175.

Poorooshasb, H.R., Holubec, I., Sherbourne, A.N., 1965. Yielding and flow of sand in triaxial compression, part I. Canadian Geotechnical Journal 3, 179–190.

Prévost, J.H., 1985. A simple plasticity theory for fractional cohesionless soils. Soil Dynamics and Earthquake Engineering 4, 9–17.

Roscoe, K.H., Schofield, A.N., Thorairajah, A., 1963. Yielding of clays in state wetter than critical. Geotechnique 13 (3), 211–240.

Vermeer, P.A., 1978. A double hardening model for sand. Geotechnique 28 (4), 413–433.

Vermeer, P.A., 1980. Formulation and analysis of sand deformation problems. Ph.D. Thesis, Delft University of Technology, The Netherlands.